

# Flow of two consecutive Taylor bubbles through a vertical column of stagnant liquid—A CFD study about the influence of the leading bubble on the hydrodynamics of the trailing one

J.D.P. Araújo, J.M. Miranda, J.B.L.M. Campos\*

Centro de Estudos de Fenómenos de Transporte, Departamento de Engenharia Química, Universidade do Porto, Faculdade de Engenharia, Rua Dr. Roberto Frias, 4200-465 Porto, Portugal

## HIGHLIGHTS

- Behaviour of the trailing bubble nose reveals a sharpening-flattening mechanism.
- Liquid film thickness of the trailing bubble increases with the bubbles approach.
- Wake region of the trailing bubble becomes larger as the bubbles are approaching.
- Numerical data on  $U/U_{SB}$  is presented for a large set of flow conditions.
- Equations and fitting parameters describing the velocity ratio curves are proposed.

## ARTICLE INFO

### Article history:

Received 19 January 2013

Received in revised form

3 April 2013

Accepted 8 April 2013

Available online 16 April 2013

### Keywords:

Hydrodynamics

Multiphase flow

Simulation

Fluid mechanics

Taylor bubble velocity

Bubble–bubble interaction

## ABSTRACT

A detailed numerical study on the interaction between two consecutive Taylor bubbles rising through vertical columns of stagnant Newtonian liquids is reported in this work. The CFD method used is based on the VOF technique implemented in the commercial package ANSYS FLUENT. Simulations were made for a large set of flow conditions, within the laminar regime, covering a range of Morton number of  $4.72 \times 10^{-5}$ –104 and an interval of Eötvös number between 15 and 575. The changes in the shape of the bubbles interface were followed throughout the approach process, and the main hydrodynamic features characterizing the liquid film and the wake region of the trailing bubble were determined as the separation distance became smaller. Numerical data on the velocity ratio between the trailing and the leading bubble are presented, and two distinct regions are identified (acceleration and deceleration) in the corresponding evolution curves. The velocity ratio curves produced for several flow conditions were fitted to equations describing the acceleration and the deceleration behaviour of the trailing bubble. These equations together with the fitting parameters obtained here can be very useful to improve simulators of continuous slug flow.

© 2013 Elsevier Ltd. All rights reserved.

## 1. Introduction

When gas and liquid flows simultaneously through a pipe, depending on the magnitude of the acting forces (inertia, buoyancy, surface tension and viscous), different phase distributions can occur, normally referred to as flow patterns. Slug flow is one of the most common gas–liquid flow patterns which take place over a wide range of flow conditions. In a vertical configuration, it is mainly characterized by a sequence of liquid slugs and elongated bullet-shaped bubbles, usually called Taylor bubbles, which occupy

most of the available cross section of the channel. The liquid in the film confined by these bubbles and the pipe wall, accelerates as it moves downwards, achieving velocities much larger than the mean values in the bulk of the liquid slugs. If the bubble is long enough, the thickness of this film decreases until the gravitational forces are balanced by the shear forces (like in a free-falling liquid film). The flow in the liquid slugs can be divided into two main parts: immediately below the rear of the bubble, where, in the majority of flow conditions, there is the formation of a recirculation/mixing region, which in laminar regime has a shape of a toroidal vortex, also called wake region; the main body of the liquid slug where the flow is gradually recovering its original and undisturbed state.

Slug flow can be observed in a variety of industrial and natural applications, such as volcanic phenomena, transportation in gas and oil pipelines, membrane processes, chemical reactors, and

\* Corresponding author. Tel.: +351 22 508 1692; fax: +351 22 508 1449.

E-mail addresses: [daraujo@fe.up.pt](mailto:daraujo@fe.up.pt) (J.D.P. Araújo),

[jmiranda@fe.up.pt](mailto:jmiranda@fe.up.pt) (J.M. Miranda), [jmc@fe.up.pt](mailto:jmc@fe.up.pt) (J.B.L.M. Campos).

microflow systems (Brill and Mukherjee, 1999; Taha and Cui, 2002; James et al., 2004; Chinnov and Kabov, 2006; Pangarkar et al., 2008; Gupta et al., 2009). Particularly relevant, due to the higher velocities in the liquid film and the recirculation/mixing in the bubble wake, slug flow pattern can have a huge interest in processes involving the enhancement of heat and mass transfer properties (Mercier et al., 1997; Leung et al., 2010; Gupta et al., 2010; Asadolahi et al., 2011; Ratkovich et al., 2011; Talimi et al., 2012). However, for example, in corrosive environments, the velocity variations described above can be undesirable, not only for the increase in the transport of corrosive species towards metal surfaces, but also by the resulting high fluctuations in wall shear stresses that cracks or, at least, complicates the formation of protective films (Villarreal et al., 2006; Zheng and Che, 2006; Nešić, 2007).

For a fully-developed continuous slug flow, the length of the liquid slugs between any pair of consecutive bubbles remains constant and long enough, so that all the bubbles are not interacting with each other, and are rising at the same translational velocity. According to Nicklin et al. (1962), under these conditions, the translational velocity can be expressed as the superposition of the drift velocity (bubble velocity in stagnant liquid,  $U_{SB}$ ) and the sum of liquid ( $U_L$ ) and gas ( $U_G$ ) superficial velocities:

$$U = U_{SB} + C(U_L + U_G) \quad (1)$$

where  $C$  is a parameter assumed to be the ratio between the maximum and the mean values of the liquid axial velocity profile, taken in the stabilized liquid ahead of the bubble nose, and so, it ranges from approximately 1.2 (for developed turbulent flows) to 2 (for developed laminar flows).

However, very large pipe lengths are necessary to achieve full development in continuous slug flow and, moreover, the occurrence of such a steady state is controversial, due to the pressure changes along the pipe and the consequent gas expansion inside the bubbles. In real systems, close to the pipe inlets, the bubbles are normally separated by small liquid slugs and thus, the influence of the wake region on the motion of the trailing bubbles cannot be avoided, which eventually leads to coalescence. Along the pipe inlet region, the developing mechanism of continuous slug flow is based on the fact that shorter liquid slugs are followed by faster travelling bubbles, and that they eventually merge forming larger individual units. The frequency of coalescence gradually decreases until, theoretically, this merging process ceases to happen.

The randomness, intermittence and unsteadiness evident in the developing slug flow pattern indicate the extremely complicated nature of the hydrodynamics involved. Due to these characteristics, a statistical approach is required to properly describe the evolution and distribution of the major flow parameters: length of the elongated bubbles; length of the liquid slugs; translational velocity of the bubbles and coalescence rate (or frequency).

Over the last years, the growing capabilities of data acquisition and processing, and the higher precision of measurement techniques, particularly the non-invasive ones, made possible the appearance of a considerable amount of research devoted to developing slug flow. Experimental studies were reported mainly for air–water systems, where the liquid slugs are fully turbulent, showing the effect of  $U_L$  and  $U_G$  in the major hydrodynamic features and, in some cases, also the influence of the pipe diameter and inclination (van Hout et al., 2001, 2002b, 2003; ; Xia et al., 2009; Mayor et al., 2008a). Only in the works of Mayor et al. (2007a, 2008b), where different aqueous solutions of glycerol were used as test fluids, can be found data for liquid slugs in the fully laminar or in a mixed scenario (laminar flow in the main body of the liquid together with turbulent wake regions). Some predictive models for the hydrodynamic parameters were also

reported, and the corresponding simulation data compared reasonably well with experimental results (Barnea and Taitel, 1993; van Hout et al., 2001; Mayor et al., 2007a, 2007b, 2008b; Xia et al., 2009). These models require the input of information about the bubble translational velocity as a function of the length of the liquid slug above it. Together with this fact, the idea that coalescence mechanisms are governed by the degree of interaction between consecutive bubbles is in agreement with all the referenced studies about continuous slug flow. Therefore, it is very important to attain a detailed knowledge about the hydrodynamics of fundamental systems, such as individual or a pair of consecutive Taylor bubbles.

Applying a dimensional analysis to the problem of an isolated Taylor bubble rising in vertical slug flow, the description can be reduced to three dimensionless groups:

- Eötvös number, representing the ratio between surface tension and gravitational effects,  $Eo = g(\rho_L - \rho_G)D^2/\sigma$ ;
- Morton number, also called the property group,  $M = g\mu_L^4(\rho_L - \rho_G)/\rho_L^2\sigma^3$ ;
- Froude number, defining the ratio of inertial and gravitational forces,  $Fr = U_{SB}/\sqrt{gD(\rho_L - \rho_G)/\rho_L}$ .

where  $\rho_L$  and  $\rho_G$  are the liquid and gas density, respectively,  $D$  the tube diameter,  $\sigma$  the surface tension, and the  $\mu_L$  the dynamic viscosity of the liquid. Other relevant dimensionless group, that can be derived from the above, is the inverse viscosity number,

$$N_f = \rho_L \sqrt{gD^3}/\mu_L = (Eo^3/M)^{1/4}.$$

Since the middle of the last century, a substantial amount of research has been dedicated to the flow of individual Taylor bubbles in vertical tubes (Dumitrescu, 1943; Davies and Taylor, 1950; Goldsmith and Mason, 1962; White and Beardmore, 1962; Collins et al., 1978; Bendiksen, 1985; Mao and Duckler, 1991). Particularly relevant to the subject of bubble–bubble interaction is the information gathered in studies more focused in the wake region. Campos and Guedes de Carvalho (1988a) performed a photographic study of the wakes of Taylor bubbles rising through stagnant liquids, varying the liquid viscosity and the tube diameter. Three different kinds of wakes were reported, depending on the inverse viscosity number: laminar and closed axisymmetric wakes for  $N_f$  below 500; a transitional regime when  $500 < N_f < 1500$ ; and open wakes with a clear turbulent behaviour and liquid shedding, for  $N_f$  higher than 1500. The same authors presented an experimental study about the mixing produced by the wake of Taylor bubbles, and compared the data with two different models (Campos and Guedes de Carvalho, 1988b). Also for a single rising bubble through a vertical column of stagnant liquid, van Hout et al. (2002a) used the Particle Image Velocimetry (PIV) to measure the velocity fields in front of the bubble, in the liquid film, and in the wake region. The system consisted of air–water, and the flow conditions were defined solely by a Reynolds number (based on  $U_{SB}$ ) of 4350. Nogueira et al. (2006) used a non-intrusive methodology combining PIV and pulsed shadow techniques (PST) to characterize the hydrodynamics of the flow in the wake region of Taylor bubbles, rising through stagnant and co-currently flowing Newtonian liquids (viscosities in the range of  $1 \times 10^{-3}$ –1.5 Pa s), inside a vertical tube with 32 mm internal diameter. Shemer et al. (2007a) extended part of the work of van Hout et al. (2002a), that related to the wake region, to other flow conditions. These different conditions were made by variations in the tube diameter (0.014–0.044 m) and in the water co-current superficial velocity (0–1 m/s).

The first research regarding the coalescence mechanism of a consecutive pair of Taylor bubbles in vertical tubes was carried out by Moissis and Griffith (1962). Pinto and Campos (1996) reported

experimental data about the approach velocities of trailing bubbles as a function of the distance to the bottom of the leading ones, flowing in vertical columns of Newtonian stagnant liquids. Different fluid properties and tube diameters were used, and pressure transducers were applied to measure the rising velocities of pairs of bubble and the distance between them. A clear limitation of this technique is that both, the velocity and the distance, are averaged between transducer taps. Later on, Pinto et al. (1998) performed a similar study for liquid flowing co-currently, with experimental conditions covering a range of Reynolds number (based on  $U_L$ ) up to 9000. Aladjem Talvy et al. (2000) studied the behaviour of trailing bubbles, in a vertical column of stagnant water, stressing the effect of the decrease of the separation distance from the leading ones. Some important features occurring in the flow of pairs of consecutive bubbles were measured by video imaging, such as the bubble shapes and translational velocities. More recently, Sousa et al. (2007) performed an experimental work regarding the interaction between Taylor bubbles in vertical columns of stagnant non-Newtonian liquids. Velocities of consecutive pairs of bubbles were measured by sets of diodes/photocells placed along a column with a diameter of 32 mm. The liquids consisted of aqueous solutions of carboxymethylcellulose (CMC) and polyacrylamide (PAA) polymers, with the purpose of getting an insight into the influence of the shear viscosity and viscoelasticity in Taylor bubble coalescence. Shemer et al. (2007b) also studied the rise of pairs of elongated bubbles through stagnant or co-currently flowing water, inside two different pipes with vertical orientation. The authors applied PIV techniques simultaneously with video imaging, in order to relate the instantaneous velocity fields in front of the trailing bubble with its shape and translational velocity.

The present paper reports a detailed numerical study about the interaction between pairs of consecutive Taylor bubbles, rising through vertical columns of stagnant liquids, based on the application of CFD tools. Several simulations were performed for systems already characterized elsewhere (Araújo et al., 2012), within the laminar flow regime, regarding the flow of individual Taylor bubbles. The study was aimed to exploit intrinsic advantages of computational methods that are related to the production of precise and extensive data, and the flexibility to easily reproduce different flow conditions. These strengths were extremely useful to overcome some of the typical issues involved with the topic under study, and to achieve a considerable amount of relevant results: (1) an important contribution is given to reduce the scarcity of available data about Taylor bubbles interaction flowing in laminar regime; (2) the behaviour of several hydrodynamic features, as the trailing bubble approaches the leading one, is extensively analysed, namely the nose and bottom bubble shapes, frontal and bottom curvature radius, liquid film thickness, wake length and volume of the trailing bubble, wall shear stress, and stabilization length of the liquid film and below the trailing bubble; (3) velocity ratio curves (curves of the ratio between the velocities of trailing and leading bubbles) are defined here for each simulated pair of Taylor bubbles, expressed by equations and parameters that vary with the flow conditions, opposing to the unique functionalities proposed in several earlier studies; (4) the analysis of the referred hydrodynamic features and the velocity ratio curves includes numerical data for very small separation distances, which is a great asset since these regions are hardly accessible to experimental techniques.

## 2. CFD model

The evolution of the flow of two consecutive Taylor bubbles, rising through vertical columns of stagnant Newtonian liquids, was simulated in the commercial CFD package ANSYS FLUENT

(Release 12.1.4). The interface tracking technique employed was based on the volume of fluid (VOF) methodology (Hirt and Nichols, 1981) already implemented in FLUENT, together with the geometric reconstruction scheme (Youngs, 1982) that assumes a piecewise-linear approach to represent the interface between phases, and the continuum surface force model (Brackbill et al., 1992) as the surface tension model. The set of governing equations arising from these considerations is detailed in the software literature.

Since the flow conditions simulated are within the laminar regime, these systems were described in two-dimensional domains with symmetry along the axis of the vertical tube, with the purpose of saving computational effort and time. Depending on the corresponding values of the minimum stabilization length below the bubble tail for single Taylor bubbles ( $L_{min,SB}$ ), presented in Araújo et al. (2012), the axial extension of the domain was 11 or 16.5 times larger than the tube diameter. The meshes consisted of a uniform distribution of quadrilateral elements, with overall densities of  $52 \times 1144$ ,  $104 \times 2288$  and  $104 \times 3432$ . To improve the accuracy and grid independence of the numerical reconstruction of the gas–liquid interface, the mesh volume elements were defined with an aspect ratio very close to one.

For each simulated system, the initial conditions were based on the corresponding numerical results of the flow field for an individual Taylor bubble (Araújo et al., 2012). Using the final data file obtained with an isolated bubble, the gas volume fraction and the velocities (axial and radial) fields, inside and around the bubble, were replicated below the bubble tail at a separation distance set between 60% and 80% of  $L_{min,SB}$ . This allowed the creation of a new data file with two identical shaped bubbles, separated by an initial desired distance ( $d_{in}$ ), which was then used as the starting point for the simulation of two consecutive Taylor bubbles.

To avoid large computational domains necessary when fixed frames are used, and the consequent time-consuming simulations, it was applied, throughout this work, moving reference frames attached to the leading Taylor bubble. This frame of reference implies that, at the top of the domain, an inlet flow boundary condition is applied, consisting of liquid phase entering the domain with a uniform velocity and equal to the velocity of the leading Taylor bubble ( $U_{in} = U_{SB}$ ). The movement of the frame of reference should also be taken into account in the tube wall boundary condition, by setting a downward velocity of the same value of  $U_{SB}$ . On the tube axis, it was assumed symmetry boundary conditions (i.e. normal gradients of all variables equal to zero). At the bottom of the computational domain, a pressure outlet boundary condition was applied, with a specified gauge pressure value taken from the corresponding numerical data obtained at the same axial position when simulating an isolated bubble (Araújo et al., 2012). This type of boundary condition was chosen due to the possibility that, in some cases, the flow of the liquid exiting the domain may not be perfectly stabilized and, consequently, a uniform velocity profile may not be fully restored.

For each flow condition numerically reproduced in this study, the value of the velocity of the leading Taylor bubble ( $U_{SB}$ ), input at the top and wall boundary conditions, was assumed equal to the numerical result obtained for an isolated Taylor bubble (Araújo et al., 2012). This assumption proved to be appropriate since, throughout the set of simulations performed, the position of the nose of the leading bubbles underwent only very small displacements. For ease of understanding, the initial and boundary conditions described are schematically represented in Fig. 1.

A pressure-based solver was chosen from the options offered in the FLUENT package, where a finite volume methodology is used to discretize the governing equations. The pressure–velocity coupling scheme applied was the pressure-implicit with splitting

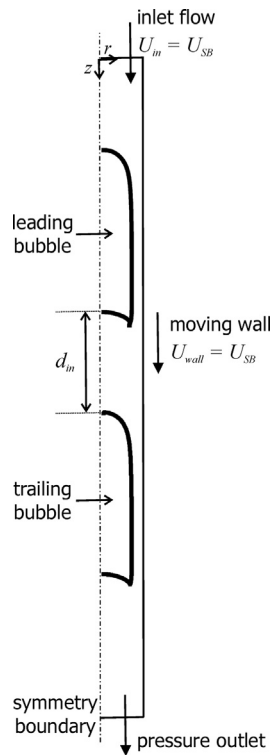


Fig. 1. Illustration of the domain, boundary and initial conditions.

of operators (PISO), and the pressure staggering option (PRESTO!) was used as the pressure interpolation method. The momentum equation was solved through the QUICK scheme, and the gradients of scalars were computed according to the Green–Gauss node-based method.

An explicit time-marching scheme was used to solve the equation for the volume fraction, where a maximum Courant number was set to 0.25, and the spatial discretization was made by the geometric reconstruction approach. This approach is widely recommended for VOF simulations, since it produces well defined interfaces, with much less numerical diffusion, when compared with other available methods. The optional implicit body force treatment was applied, since when simulating multiphase flows with large body forces, like gravity acting on phases with high density differences, it is advisable to use it for avoiding convergence problems and guarantee more robust solutions. A global Courant number was also set to 0.25, which controlled the variable time step used in the resolution of the governing equations. In each time step, the maximum number of iterations was 1000. The velocities and continuity scaled absolute values of the residuals were monitored and set to  $10^{-6}$  for the convergence criterion.

### 3. Results and discussion

When two Taylor bubbles flow consecutively, the leading one has a strong influence on the hydrodynamic behaviour of the trailing bubble. This influence is exerted through the velocity field that is induced by the movement of the leading bubble in the liquid phase below it, which gets more pronounced in the near wake region. For this reason, it is particularly interesting to access information on bubble interaction as the separation distance between them becomes shorter. Due to the clear difficulties of available experimental techniques on performing reliable measurements in such small and fast displacements, the CFD capabilities were exploited with the purpose of obtaining a detailed

description of the approach and pre-merging process between Taylor bubbles.

Simulations were performed for a set of different flow conditions, within the laminar regime and for stagnant liquid, in order to understand the role of the relevant forces involved. This variation in the flow conditions can be expressed by different pairs of Morton and Eötvös numbers. With the purpose of providing a simple overview of the role of flow conditions in the evolution of the liquid flow field and bubbles shape, different sequential images representing numerical data of gas–liquid interfaces and streamlines, as the approach process evolves, are gathered in the following illustrations.

In Fig. 2, the behaviour of the gas–liquid interfaces of pairs of consecutive bubbles and the streamlines in the surrounding liquid can be observed, as the dimensionless separation distance based on the column diameter ( $d/D$ ) decreases. The figure shows five different simulated systems where the Morton number varies between  $4.72 \times 10^{-5}$  and 104, and the value of  $Eo$  remains approximately constant. Two aspects are clear, and should be pointed out first: the presence of a recirculation zone below the bubbles bottom depends on the Morton number, and generally appears at lower values of  $M$ ; as the Morton number decreases, a noticeable bubble–bubble interaction occurs at larger separation distances. These aspects only reflect the behaviour of the wake region of an isolated bubble and the minimum stabilization length below its bottom ( $L_{min,SB}$ ), already reported in Araújo et al. (2012), and are not a direct consequence of the interaction between the consecutive Taylor bubbles. As it was expected, the shape and position of the nose of the leading bubble remains unaffected by the approach of the trailing bubble and also by the change in the dimensionless property group. Conversely, the nose shape of the trailing bubble seems to be very sensitive to its distance from the bottom of the leading bubble, with this sensitivity increasing as the Morton number decreases. Apparently, the flow field in the liquid phase between bubbles induces a stretching of the trailing bubble through its upper end, which is reflected in its nose shape and displacement. The deformation of the trailing bubble nose is highly pronounced for the systems with lower  $M$ , in particular when it enters the wake region of the leading bubble, which can cause the development of a neck-shaped zone in the body of the trailing bubble. From the observation of Fig. 2, there are some features where doubts still remain about their dependence on the separation distance between bubbles and the flow conditions, namely the bottom shape of the two bubbles, and the liquid film thickness and wake dimensions of the trailing bubble. A deeper analysis is presented in the following sections that will help to clarify the behaviour of these features.

Similarly to the procedure applied in Fig. 2, numerical results of gas–liquid interfaces and streamlines obtained in the simulation of a pair of Taylor bubbles in four different flow conditions are illustrated in Fig. 3. These flow conditions have an identical Morton number ( $4.72 \times 10^{-5}$ ) and a  $Eo$  ranging from 34 to 106, to check on the relevance of the later dimensionless group in the bubbles approach process. Simplifying the qualitative observations taken from Fig. 3, it can be said that they are analogous to those outlined from Fig. 2, if the effect of a decreasing  $M$  is replaced by the influence of an increasing  $Eo$ . The same questions also arise about the behaviour of the bottom shapes, and a possible thickening of the liquid film together with an enlargement of the wake region of the trailing bubble, as the distance between bubbles decreases. These unanswered issues and the necessity to improve the characterization of bubble–bubble interactions justify the importance of gaining a deeper insight into the evolution of several hydrodynamic features.

The referred analysis is presented in the following sections, and was mainly focused on two flow conditions using the extreme



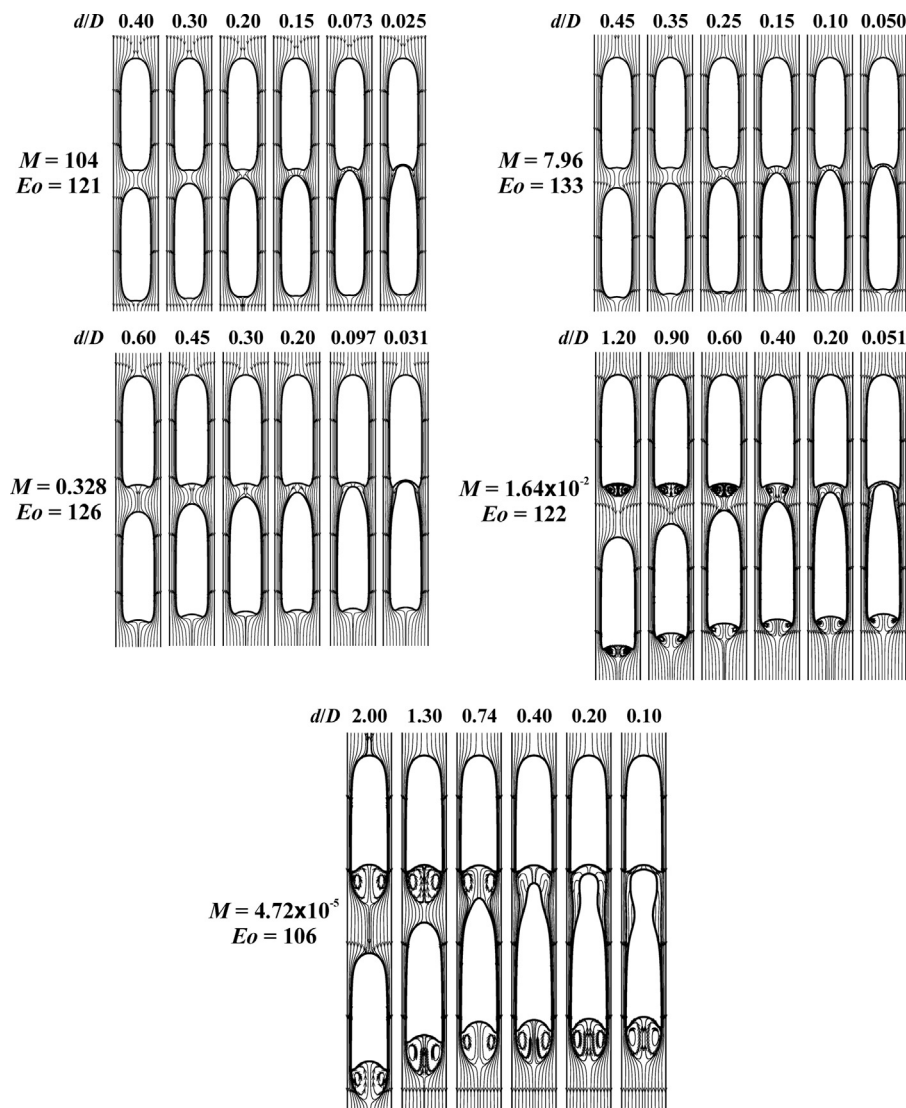


**Fig. 2.** Numerical data of the bubbles interface and streamlines in the liquid phase, as a function of  $d/D$ , for systems with different  $M$  and  $Eo$  around 121.

values of  $M$  under study (Condition A— $M=104$  and  $Eo=121$ ; Condition B— $M=4.72 \times 10^{-5}$  and  $Eo=85$ ). This careful analysis is divided into three parts: determine the degree of disturbance suffered by the shape of the bubbles extremities; confirm an hypothetical alteration of the developed liquid film and related parameters in the trailing bubble; evaluate a possible increase of the wake region and stabilization length below the trailing bubble when compared with the dimensions reported for the flow of an individual Taylor bubble (Araújo et al., 2012). To conclude the results presentation, a section is devoted to the evolution of the bubbles velocity, in the entire range of simulations performed, since this is probably the most useful hydrodynamic feature to extract from this kind of gas–liquid system, considering the application point of view of better understanding and predicting the development of continuous slug flow.

### 3.1. Shape of the gas–liquid interface

The deformation suffered by the original shape of a single Taylor bubble, when placed under the influence of a second bubble, is perhaps the most evident aspect that stands out from a raw observation of the numerical data obtained. Focusing on the regions of the gas–liquid interface near the extremities of the leading and trailing bubble, the simulation results regarding both

conditions under investigation (A and B) are addressed with more detail in this section.

As pointed out above, the idea that the nose of the leading bubble remains undisturbed was confirmed through a closer analysis of the evolution of its shape. For both flow conditions, it is very clear that the nose of the leading bubble reveals a steady behaviour throughout the bubbles approach process, and is perfectly similar to the shape of the nose of a Taylor bubble when flowing isolated and under the same conditions.

Regarding the extremities directly involved in the coalescence process (bottom of the leading bubble and nose of the trailing bubble), the results concerning the gas–liquid interface position are presented in Fig. 4. To give a better visual image of the approach process, for both flow conditions, the evolution of the position and shape of the leading bubble bottom and of the trailing bubble nose are placed side by side. The reference point for the dimensionless axial position ( $z/D$ ) in Fig. 4 was placed on the tip of the nose of the leading bubble, considering that this position is approximately constant throughout each simulation. For consistency purposes, this kind of reference point was also applied in the following figure concerning the shape of the trailing bubbles bottom (Fig. 5). Within each flow condition, the scale dimensions of the axial ( $z/D$ ) and radial ( $r/D$ ) positions were made dependent and with a ratio of 1, to ensure that the illustrated

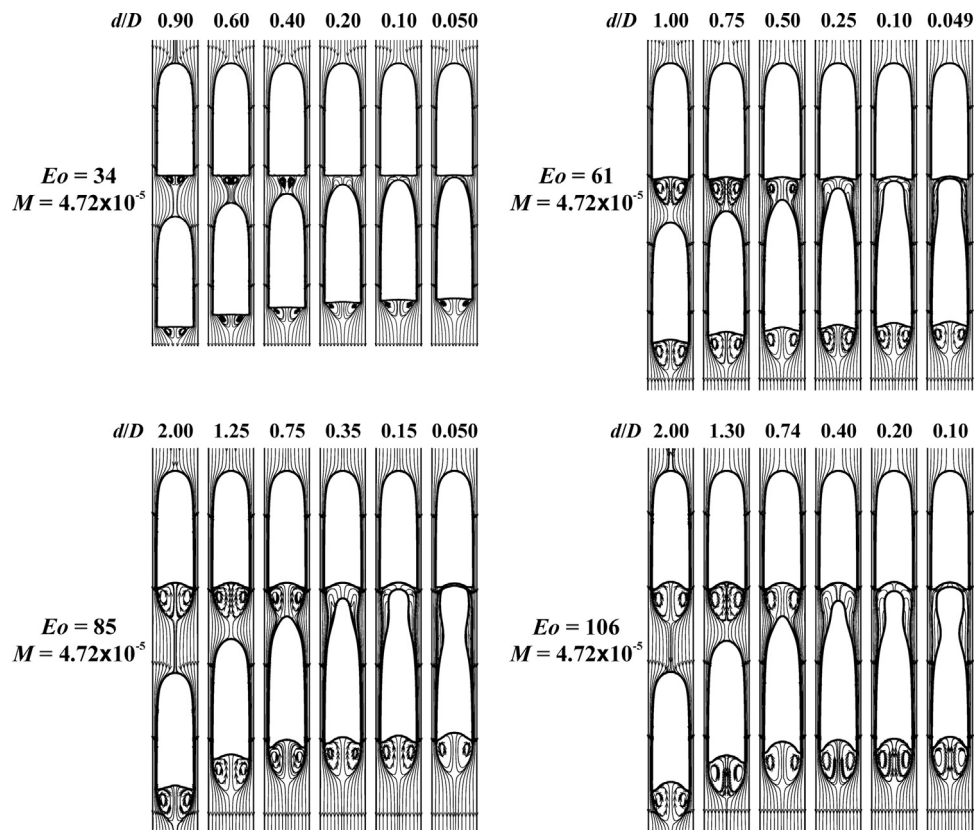


**Fig. 3.** Numerical data of the bubbles interface and streamlines in the liquid phase, as a function of  $d/D$ , for systems with similar  $M$  ( $4.72 \times 10^{-5}$ ) and  $Eo$  varying between 34 and 106.

shapes exhibit a correct proportion between both coordinates. To respect this unity ratio, it is relevant to note that the ordinates axis for condition B occupies a shorter space in Fig. 4, since this flow condition is characterized by larger axial influence zones, and so, the  $z/D$  axis must cover a wider range than the corresponding one in condition A.

As was previously stated, in Fig. 4 it is confirmed that the most noticeable shape alteration occurs in the trailing bubble nose and for the condition with the lower Morton number (condition B). This alteration is accompanied by a larger displacement of the  $z/D$  coordinate of the nose tip. In the first stages of the trailing bubble approach, the tip of its nose tends to sharpen until it reaches a separation distance between approximately 10% and 20% of the corresponding minimum stabilization length below an isolated bubble ( $L_{min,SB}$ ). At that point, the behaviour of the trailing bubble nose suffers a visible change, since its shape begins to flatten as it moves to regions very close to the bottom of the leading bubble. This kind of sharpening-flattening evolution of the trailing bubble nose is shared by both flow conditions under analysis, although it seems to be more drastic in condition B. However, also for this flow condition, along with the deeper flattening observed it is noticed the development of a neck in the gas–liquid interface of the trailing bubble, just below its nose region. As the trailing bubble approaches the leading one, the neck minimum width decreases and gets further distanced from the tip of the nose. The behaviour registered in this neck development seems to suggest that, if the Morton number is further reduced, the trailing bubble can be fragmented before its coalescence with the leading bubble. This hypothesis is not tested here, since lowering the values of  $M$  would lead to conditions outside the laminar regime, which is not within the scope of the present study.

When discussing Figs. 2 and 3, an issue that was left to be further explained was the possibility of the leading bubble bottom

being deformed during the approach process, and also if the flow conditions have any influence on that eventual deformation. Based on Fig. 4, a closer insight can be performed, which clarifies any uncertainty about the referred issue. It becomes clear that the bottom of the leading bubble is substantially deformed when the surrounding liquid has a higher viscosity (condition A), whereas for a lower Morton number (condition B) the bottom shape is only slightly altered when the bubbles are very close to merging. The physical interpretation behind these opposing behaviours is related with the fact that, as the viscous forces are increased, the draining of the liquid present between both bubbles through the film of the trailing one becomes more difficult. It implicates that the shape of the leading bubble bottom must then deform more markedly to accommodate this growing handicap to liquid drainage.

To infer about the influence of the bubbles approach process on the evolution of the rear end of the trailing bubble, the corresponding gas–liquid interface data are presented in Fig. 5. From this illustration, it is simple to conclude that, for both flow conditions under analysis, the bottom of the trailing bubble only suffers a displacement effect, which is inherent to the dislocation of this bubble towards the leading one. Concerning the shapes of this bubble extremity, they remain approximately constant and similar to the ones obtained by numerical simulation of isolated Taylor bubbles (Araújo et al., 2012).

With the purpose of introducing some quantification into the discussion above, the curvature radius of three different extremities were tracked throughout the bubble approach process: bottom of the leading bubble; nose and bottom of the trailing bubble. The determination of these data were made for conditions A and B, following simple methods already described elsewhere (Araújo et al., 2012), and the results obtained are gathered in Fig. 6. For a better perception of the deviation found from the

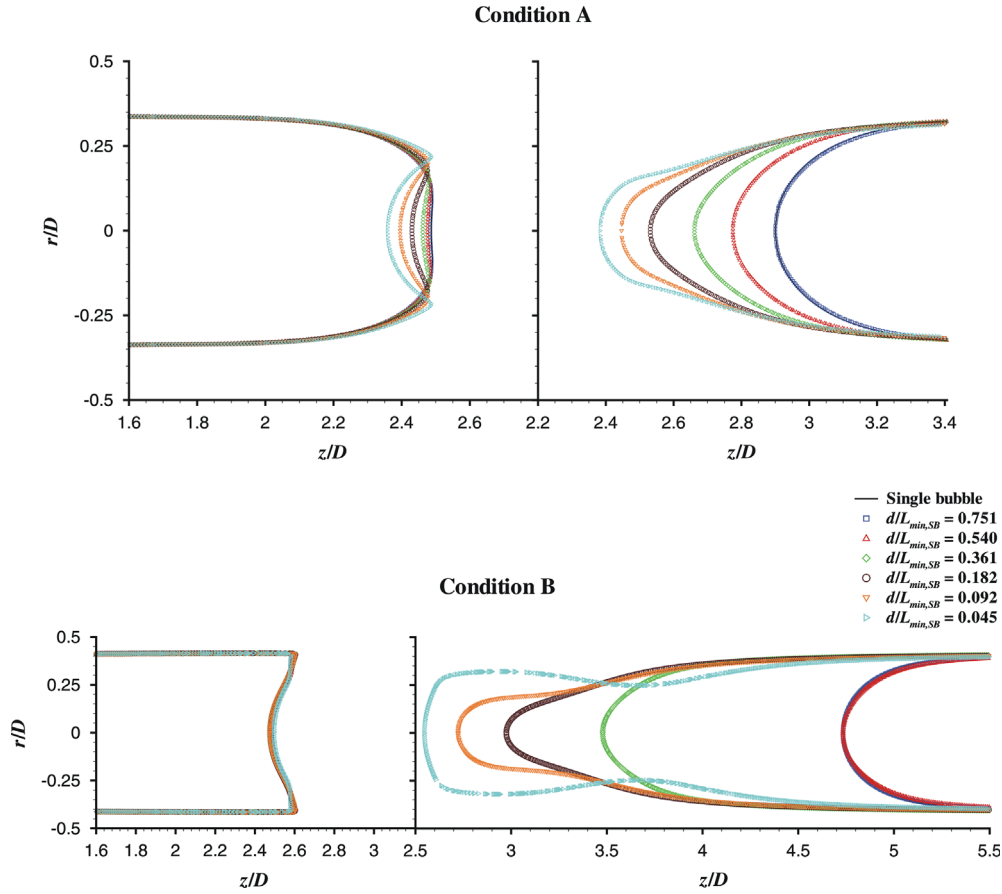


**Fig. 4.** Evolution of the shape and position of the leading bubble bottom and the trailing bubble nose with  $d/L_{min,SB}$  (symbols), for conditions A and B. The corresponding shapes obtained in the simulations of single bubble systems (Araújo et al., 2012) are also presented (solid lines). The origin of the axial coordinate is placed at the tip of the leading bubble nose.

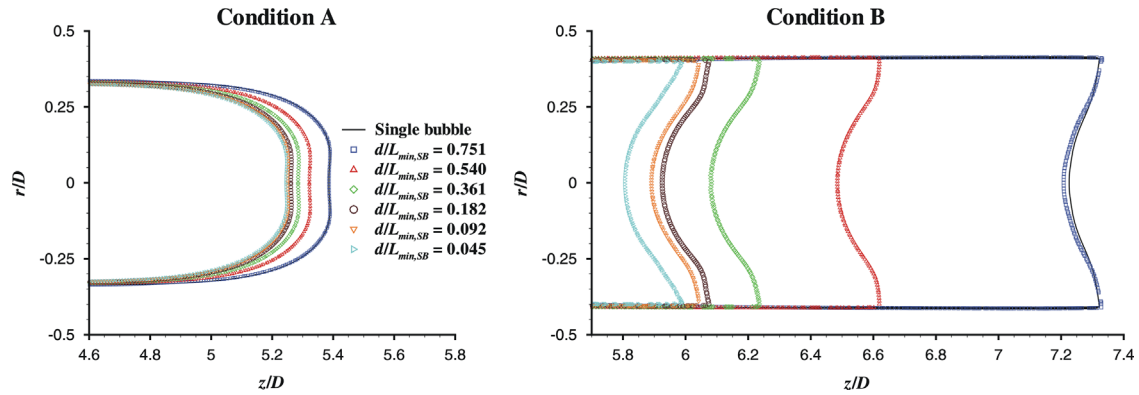


**Fig. 5.** Evolution of the shape and position of the trailing bubble bottom with  $d/L_{min,SB}$  (symbols), for conditions A and B. The corresponding shapes obtained in the simulations of single bubble systems (Araújo et al., 2012) are also presented (solid lines). The origin of the axial coordinate is placed at the tip of the leading bubble nose.

corresponding numerical data related with the flow of an isolated Taylor bubble, the results are presented in fraction form between the bottom ( $R_B$ ) or the nose ( $R_F$ ) curvature radius obtained here and the bottom ( $R_{B,SB}$ ) or the nose ( $R_{F,SB}$ ) curvature radius achieved in single bubble systems (Araújo et al., 2012). In order to allow a direct graphical comparison between the data regarding both flow conditions under the spotlight, the dimensionless separation distance normalized by the minimum stabilization length below the bottom of an isolated bubble ( $d/L_{min,SB}$ ) was applied as the x-coordinate throughout Fig. 6.

Examining the results presented in Fig. 6 with some care, it is easy to notice that they corroborate the observations made about Figs. 4 and 5, when discussing the qualitative behaviour of the three extremities at stake (tail of the leading bubble; nose and bottom of the trailing bubble). This conclusion is supported in the following thoughts:

- the results concerning the simulation of condition A express that the bottom curvature radius of the leading bubble suffers a large and constant decrease throughout the bubbles approach

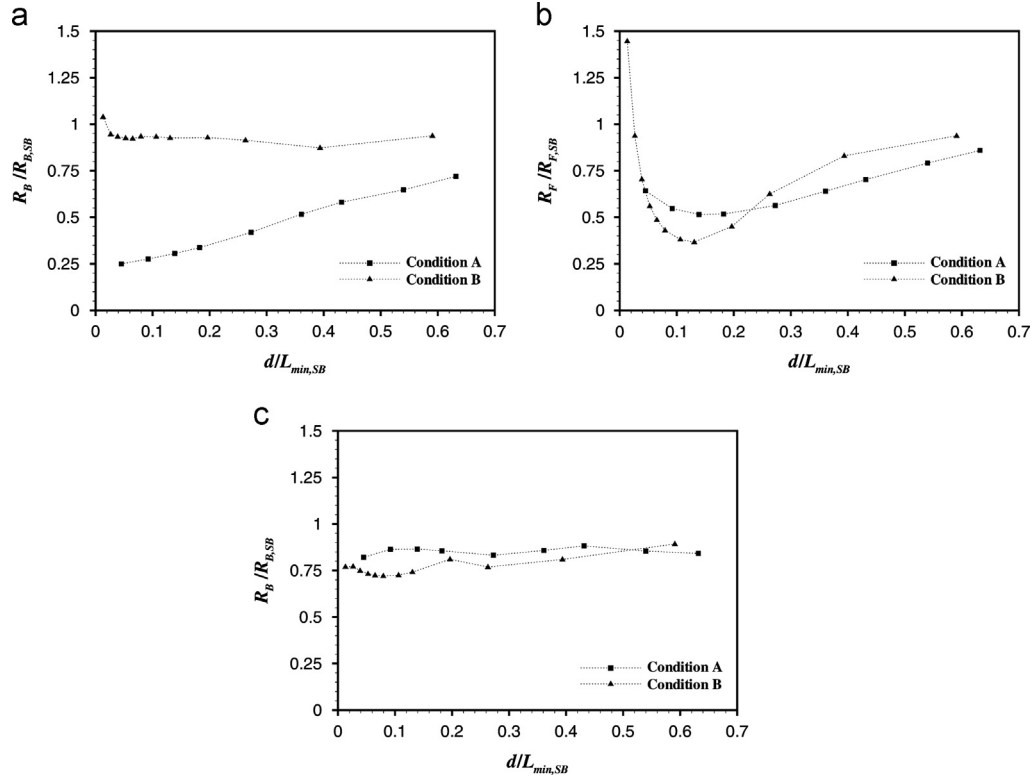


**Fig. 6.** Numerical data on the curvature radius, as a function  $d/L_{min,SB}$ , obtained for conditions A and B, and for three different bubbles extremities: (a) leading bubble bottom; (b) trailing bubble nose; and (c) trailing bubble bottom. The results are presented in a fractional form of the corresponding values for single bubble systems.

process. On the other hand, the values of  $R_b/R_{B,SB}$  of the leading bubble, flowing under condition B, exhibit an almost complete steadiness, only disturbed by a sudden increase at very small separation distances. The occurrence of these opposing behaviours in the leading bubble rear end, when the viscosity of the surrounding liquid is substantially changed, was previously detected and explained in the discussion of Fig. 4.

- for conditions A and B, the frontal curvature radius of the trailing bubble decreases, as the bubbles get closer, until the separation distance ( $d/L_{min,SB}$ ) is around 0.1–0.2, which coincides with the period of nose sharpening observed in Fig. 4. Then, the evolution of the curvature radius inverts its tendency, and the values start to increase, confirming the nose flattening for small separation distances. Also, as was claimed above, the nose behaviour just described is more accentuated for lower  $M$  (condition B), which agrees with a corresponding higher data variation in Fig. 6b.
- the results of the bottom curvature radius of the trailing bubble reflects only small oscillations with a decrease of the separation distance between bubbles and inside the  $d/L_{min,SB}$  interval under analysis (from around 0.05 to 0.7). This observation is verified for both flow conditions. The plateaux of  $R_b/R_{B,SB}$  in Fig. 6c remain close to 0.80–0.85, which is a 15–20% deviation from the shape of a single bubble flowing under the same conditions. This minor difference is possibly caused by a slight variation in the shape of the trailing bubble bottom, for radial positions very close to the column centreline, occurring at  $d/L_{min,SB}$  between 0.8 and 1.0, which is outside the scope of separation distances defined for this study.

### 3.2. Liquid film of the trailing bubble

Due to the movement of the trailing bubble towards the leading one, and the consequent displacement of liquid between

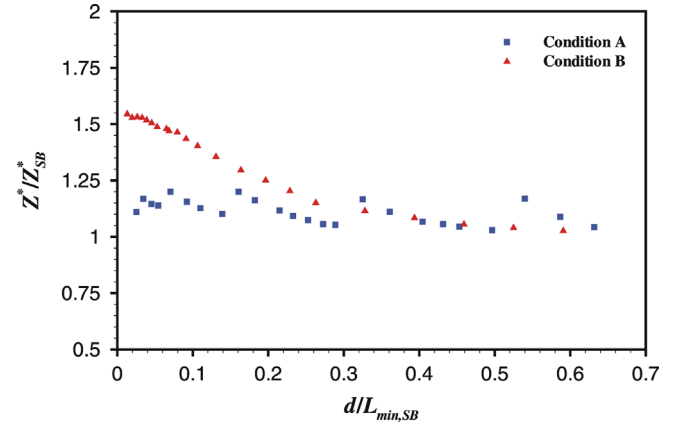


**Fig. 7.** Numerical results of  $Z^*/Z_{SB}^*$  as a function  $d/L_{min,SB}$ , obtained for conditions A and B.

the two bubbles, it is expected that the hydrodynamic features in the liquid film region of the trailing bubble suffers some adjustments to accommodate the changes caused by this unsteady state. An inspection about the nature of these adjustments is now presented, based on the results of the simulations regarding conditions A and B.

Starting by the length necessary to achieve a state of fully developed film ( $Z^*$ ), in both conditions, the numerical results were converted into fractions of the corresponding length obtained for isolated bubble systems ( $Z_{SB}^*$ ), and are illustrated in Fig. 7 as a function of the dimensionless separation distance based on  $L_{min,SB}$ .

Looking at Fig. 7, it is clear that, for the flow condition with lower Morton number (condition B), the length of the developing liquid film increases continuously, and up to 55% of the original value of  $Z_{SB}^*$ , as the two bubbles are approaching. On the other



hand, concerning condition A, it seems that this stabilization length is not relevantly influenced by the bubbles separation distance, and is kept around an average  $Z^*/Z_{SB}^*$  value of 1.11. Although the  $Z^*/Z_{SB}^*$  data for condition A shows some tendency to oscillate throughout the approach process, the behaviour of this stabilization length is considered approximately constant, since it results from an inflation of a small amplitude numerical wave in the corresponding results of  $Z'$  amplified by the large difference between the  $Z_{SB}^*/D$  values of both flow conditions—0.926 for condition A and 2.086 for condition B (Araújo et al., 2012). When comparing the  $Z^*/Z_{SB}^*$  data of both flow conditions under analysis, the apparent opposing behaviour can be related to the different trailing bubble velocity and the amounts of liquid being displaced between bubbles. In condition B, the amount of liquid between bubbles and the trailing bubble velocity achieves higher values than in condition A, as it will be shown in Section 3.4, which leads to increased levels of liquid flow rate to be drained through the liquid film. These higher increments in the liquid flow rate of condition B, which is also discussed and presented in later illustrations, generates more difficulties to stabilize the flow in the liquid film and causes a growing necessity for larger extensions of tube to achieve a fully development state.

The results of  $Z'$  gathered in Fig. 7 were determined by the application of a quantitative criterion already defined elsewhere (Araújo et al., 2012). This criterion is based on the velocity data obtained at the radial midpoint of the fully developed film. To visualize how the stabilization of the referred data is reached, the dimensionless axial velocity ( $u_z/U_{SB}$ ) is presented in Fig. 8 at different separation distances and for the two flow conditions. The origin of the axial coordinate ( $z$ ) was placed at the tip of the trailing bubble nose, and the values of  $u_z$  were converted to a frame of reference attached to the wall, i.e., a fixed frame of reference (FFR).

Common to both flow conditions, the behaviour of the  $u_z/U_{SB}$  curves near the tip of the trailing bubble nose suffers an inversion at a  $d/L_{min,SB}$  around 0.15–0.20. For higher separation distances, the axial velocity exhibits an increase tendency throughout the developing film region, in accordance to what occurs in the corresponding region of an isolated Taylor bubble. This is simply due to a decreasing cross-sectional area available for the liquid flow, delimited by the wall and the interface of the trailing bubble, which promotes a liquid acceleration up to the axial position where a fully developed state is reached. For small distances between bubbles, the axial velocity data close to the nose tip shows a deceleration region that increases its length as the two bubbles gets closer, and is much more pronounced in the results of condition B. The main cause of this behaviour is the proximity of the trailing bubble to locations where the liquid jet exiting the film of the leading bubble is not fully expanded, which demands to be further decelerated below the nose tip of the trailing bubble.

The  $u_z/U_{SB}$  curves for condition A reveal relatively stable plateaux, at  $z/D$  between 1 and 2, which is an indisputable indication that, independently of the distance separating the pair of bubbles, the simulation data incorporates a well-developed liquid film region in the trailing bubble. These curves also include some waves almost undetectable that, as previously discussed, are translated in the oscillations observed in the  $Z^*/Z_{SB}^*$  results.

Looking at the  $u_z/U_{SB}$  data obtained for condition B, the stabilization of the film is not so evident as the one for condition A. Particularly, these doubts are more pertinent for separation distances below 10% of  $L_{min,SB}$ , and it could be argued that a simulation of condition B with longer bubbles would be required to completely assure stabilization. However, the stabilization criterion applied is fulfilled in all the numerical data analysed and, in the more extreme situation presented in the right graph of Fig. 8 ( $d/L_{min,SB} = 0.013$ ), below the axial position where it was determined to reach a fully developed film, the bubble has a length of more than  $0.2D$  until is reached the lower tip of the trailing bubble tail. Due to these considerations, it was assumed that the results gathered in Fig. 8 are reasonably correct and that, with an acceptable margin of error, the liquid film of the trailing bubbles always reaches a fully developed state during the entire simulation procedure. This assures that, even for the simulation of condition B, it is safe to carry through a deeper analysis about the hydrodynamic features related to the developed liquid film of the trailing bubble, without repeating the simulation using longer bubbles.

The trailing bubble velocity and the amount of liquid between bubbles that is drained through the developed film are the key players in the behaviour of the hydrodynamics within this flow region. The effect of this liquid drainage is translated by an additional flow rate ( $\Delta Q$ ) that is expected to depend on the separation distance between bubbles and on the flow conditions. The numerical data of  $\Delta Q$  obtained for conditions A and B is divided by the liquid flow rate that passes through the film of an isolated bubble ( $Q_{in}$ ), considering a frame of reference moving with the leading bubble (MFR), and is presented as a function of the dimensionless separation distance ( $d/L_{min,SB}$ ) in the lower graph of Fig. 9. This liquid flow rate ( $Q_{in}$ ) is calculated by

$$Q_{in} = U_{SB}\pi R^2 \quad (2)$$

The values of the additional flow rate ( $\Delta Q$ ) were estimated by numerical integration of simulation data obtained in axial iso-surfaces belonging to a region where the liquid film of the trailing bubbles were assumed to be fully developed:

$$\Delta Q = \int_{R-\delta}^R u_z 2\pi r dr - Q_{in} \quad (3)$$

where  $\delta$  is the thickness of the developed film and  $u_z$  is used in MFR.

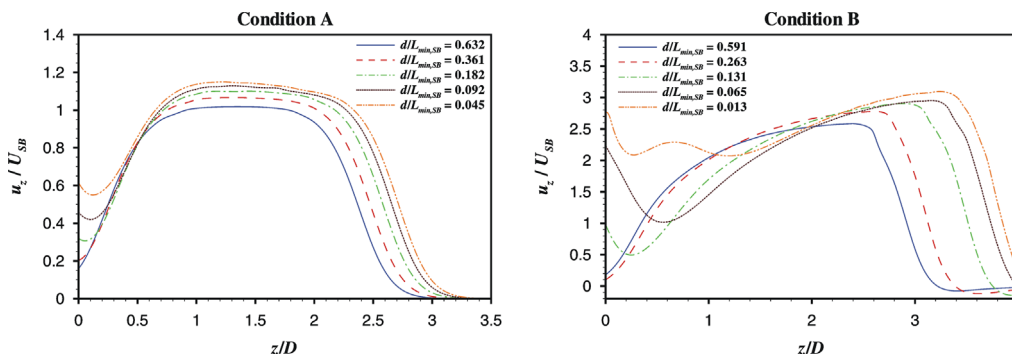
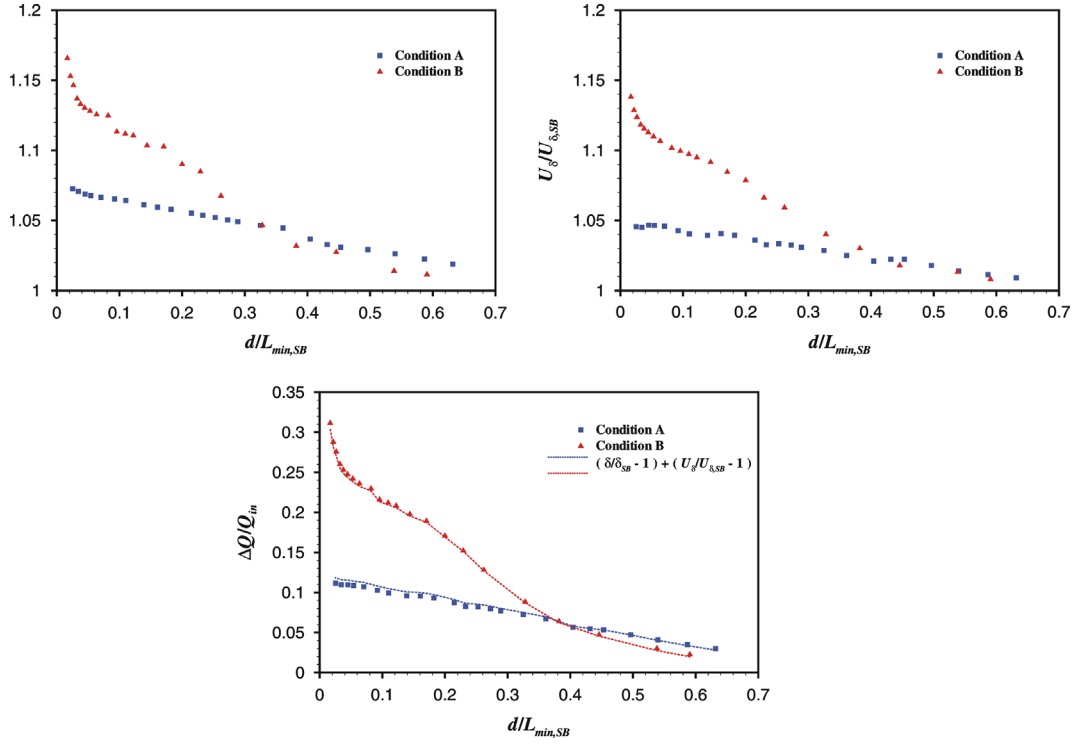


Fig. 8. Results of the dimensionless axial velocity ( $u_z/U_{SB}$ ) as a function of  $z/D$ , for conditions A and B at several  $d/L_{min,SB}$ . The data was taken for radial iso-surfaces in the midpoint of the developed liquid film of the trailing bubble, and the origin of the axial coordinate is placed at the tip of the trailing bubble nose.



**Fig. 9.** Numerical data on the main hydrodynamic features of the developed liquid film of the trailing bubble, obtained for conditions A and B, as a function  $d/L_{\min,SB}$ : (a) thickness of the liquid film (upper left graph); average axial velocity of the liquid in the film (upper right graph); and additional flow rate due to the liquid drainage between bubbles (lower graph). The results are presented in a fractional form of the corresponding values for single bubble systems.

Similarly to the illustration made for  $\Delta Q$ , the liquid film thickness ( $\delta$ ) and the average velocity inside the developed film ( $U_\delta$ ) are also shown in the upper graphs of Fig. 9. These hydrodynamic features were converted into fractions of the corresponding values regarding the flow of an individual bubble ( $\delta_{SB}$  and  $U_{\delta,SB}$ ). The data of  $U_\delta$  was determined by the following equation:

$$U_\delta = \frac{\int_{R-\delta}^R u_z 2\pi r dr}{\pi R^2 - \pi (R-\delta)^2} \quad (4)$$

For both flow conditions, in Fig. 9 can be observed that  $\Delta Q$  is dependent on  $d/L_{\min,SB}$ , since it increases throughout the bubbles approach process. Theoretically, in the liquid film region of the trailing bubble, it is expected that the system instantaneous response to accommodate this flow rate variation should be based on two features—an increase of the liquid film thickness, and an increase of the average velocity of the liquid flowing downwards through the developed film. As can be seen in Fig. 9, the simulation results confirm this expectations, since the evolution of the  $\delta/\delta_{SB}$  and  $U_\delta/U_{\delta,SB}$  data, for conditions A and B, reveal a behaviour very similar to  $\Delta Q/Q_{in}$ . Furthermore, the perturbation introduced in the liquid film of the trailing bubble by  $\Delta Q$  is, roughly speaking, evenly distributed between  $\delta$  and  $U_\delta$ : for condition A, maximum values around 7% and 5% above of the corresponding data obtained with a single bubble were detected for  $\delta$  and  $U_\delta$ , respectively; for condition B, the numerical data of  $\delta/\delta_{SB}$  and  $U_\delta/U_{\delta,SB}$  reaches 1.17 and 1.14, respectively, which corresponds to maximum deviations of 17% and 14% from the original state of isolated bubble.

The dotted lines placed in the illustration of the  $\Delta Q/Q_{in}$  data were built using the fractional deviations of  $\delta$  and  $U_\delta$  from the corresponding values for single bubble, which can be extracted from the upper graphs of Fig. 9. The only intention is to highlight the known concept that the sum of these deviations should be approximately equivalent to the fraction of the flow rate resulting from the liquid drainage between bubbles ( $\Delta Q$ ), since the flow rate

in the liquid film is essentially dependent on the arithmetic product of its thickness by the average velocity flowing through it.

As was pointed out in the discussion of the results of  $Z'$ , as the trailing bubble approaches the leading one, it is obvious from Fig. 9 that, when compared with condition A, the successive increments to the additional flow rate  $\Delta Q$  are much higher in condition B. This difference is translated not only in the order of magnitude of the  $\Delta Q/Q_{in}$  values, but also in the apparent functionality with  $d/L_{\min,SB}$  that these sets of data seem to follow—linear for condition A and negative exponential for condition B. The exact same conclusions can be taken from the  $\delta/\delta_{SB}$  and  $U_\delta/U_{\delta,SB}$  results, when comparing data between both flow conditions.

The evolution of the wall shear stress along the column and throughout the bubbles approach process is another hydrodynamic feature that deserves a considerable degree of attention, since in slug flow it is strongly related to the bubbles shape and position. This kind of information can be particularly useful for processes involving heat or mass transfer phenomena. Due to the constriction of the cross-sectional area available for the liquid flow, the higher velocity levels are achieved in the liquid film, which is synonymous of significantly larger wall shear stress values in this flow region.

To better understand the role of the bubble–bubble interaction in the wall shear stress ( $\tau_w$ ) behaviour, and the effect of changing the flow conditions, the evolution of the dimensionless wall shear stress ( $\tau_w/(\rho_L g D)$ ) along the axial coordinate is presented in Fig. 10 for several separation distances within each flow condition under analysis. The origin of the dimensionless axial coordinate ( $z/D$ ) was placed at the tip of the leading bubble nose. It is also important to notice that the positions of the bubbles extremities, taken along the column axis, are marked with filled circular points, and the  $\tau_w/(\rho_L g D)$  data concerning the regions between these extremities are represented by the thicker lines.

The wall shear stress data corresponding to the presence of the leading bubble remains almost unchanged throughout the bubble

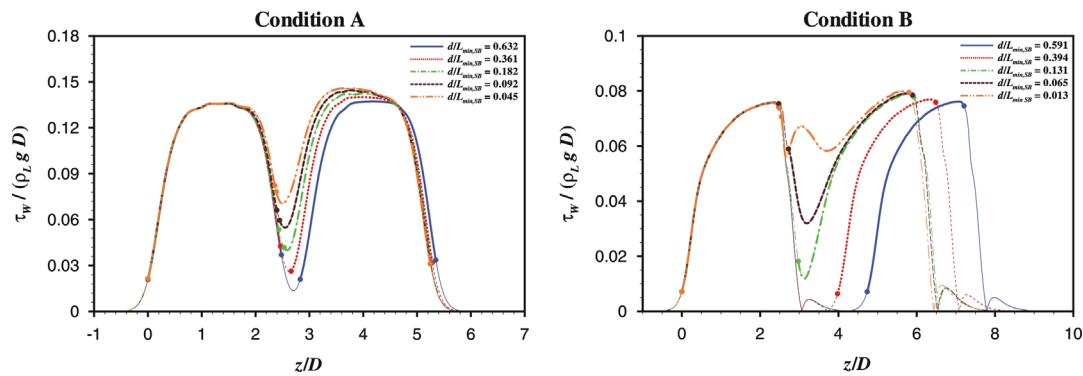


**Fig. 10.** Results of the dimensionless wall shear stress as a function of  $z/D$ , for conditions A and B at several  $d/L_{min,SB}$ . The position of the bubbles' extremities are marked with filled circular points, and the wall shear stress data in the regions inside these positions are represented with thicker lines. The origin of the axial coordinate is placed at the tip of the leading bubble nose.

approach process, which can be confirmed by the lines overlapping in an interval of  $z/D$  around  $-1$  and  $2$ , observed in both graphs of Fig. 10. Regarding the influence of the trailing bubble in  $\tau_w/(\rho_l g D)$ , it follows the same trends already discussed for the  $u_z/U_{SB}$  data taken throughout the column at the radial midpoint of the developed liquid film. The conclusions should be similar since, besides the fluid viscosity, the wall shear stress essentially depends on the axial velocity in the vicinity of the wall. The maximum wall shear stress values increase as the trailing bubble approaches the leading one, reflecting the same tendency of the axial velocity within the trailing bubble liquid film. Based on the data of Fig. 10, when compared the corresponding values obtained for an isolated bubble, it was determined a 7.8% and a 5.8% increase of the maximum  $\tau_w/(\rho_l g D)$  for conditions A and B, respectively. Again, it must be emphasized that the sudden tendency changes observed in the  $\tau_w/(\rho_l g D)$  curves, due to the influence of the bubbles' dislocation in the liquid flow near the wall, are very important and may perform a dominant role in situations where heat or mass transfer occur simultaneously with slug flow.

### 3.3. Wake of the trailing bubble

The disturbances caused by the continuous and unsteady displacement of the trailing bubble towards the leading one, together with the liquid drained between the bubbles ( $\Delta Q$ ), are determinant in the hydrodynamics of the trailing bubble surroundings, not only regarding  $Z^*$  and the features related to the developed liquid film ( $\delta$  and  $U_\delta$ ), but they are also reflected upstream with particular emphasis in the wake region. To confirm this fact, a detailed analysis of the hydrodynamic features characterizing the flow below the trailing bubble was performed concerning condition B since, from the two flow conditions under detailed investigation it is the only one where a recirculation zone was detected.

Starting with the length necessary, behind the trailing bubble, to have an undisturbed state ( $L_{min}$ ) in the liquid – for stagnant liquid corresponds to zero velocity in FFR or an axial velocity equal to  $U_{SB}$  in MFR – some numerical data of  $L_{min}$ , obtained throughout the approach process, were normalized by the corresponding stabilization length for a single bubble (Araújo et al., 2012) and are presented in Fig. 11.

The simulation data of  $U_\delta/U_{\delta,SB}$ , previously shown in Fig. 9, was also placed in Fig. 11 with the purpose of finding a direct connection between the growing separation of  $U_\delta$  from  $U_{\delta,SB}$  and some possible deviations, from  $L_{min,SB}$ , of the stabilization length below the trailing bubble; these latter deviations are determined through a criterion (Araújo et al., 2012) that depends on the axial velocity in the column centreline. Disregarding for a moment the

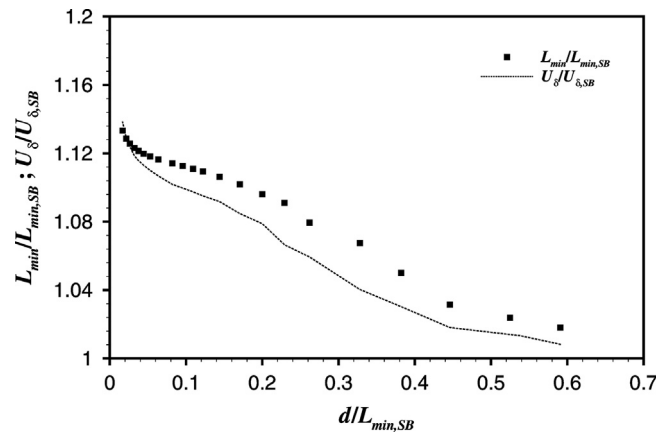


**Fig. 11.** Numerical results of  $L_{min}/L_{min,SB}$  as a function  $d/L_{min,SB}$  (symbols), obtained for condition B. The data of  $U_\delta/U_{\delta,SB}$  (dotted line) is also represented for comparison purposes.

detachment between the points and the dotted line seen in Fig. 11, the closeness between the ranges of the  $L_{min}/L_{min,SB}$  and  $U_\delta/U_{\delta,SB}$  values, and the similarity in the evolution of these two dimensionless features as the bubbles are approaching, clearly indicates that the perturbations felt by the average velocity within the liquid film are continuously transmitted to the stabilization length below the trailing bubble. The referred detachments between the line and points in Fig. 11 are, most probably, owed to a variation in the dimensions of the recirculation zone. These variations in the wake dimensions affect the cross-sectional areas available in the downward path of the liquid in expansion at the exit of the liquid film, which introduces another source of disturbance to the velocity profiles below the wake.

Based again on the simulation data obtained for condition B, the wake dimensions of the trailing bubble were determined to verify the existence of some dependence on the separation distances between bubbles. The collected data on the trailing bubble wake length ( $L_w$ ) and volume ( $V_w$ ) was normalized by the corresponding values obtained for single bubble (Araújo et al., 2012),  $L_{w,SB}$  and  $V_{w,SB}$ , respectively, and are compiled as a function of  $d/L_{min,SB}$  in Fig. 12.

Due to the continuous changes of the relative velocity between the trailing bubble and the liquid exiting its film (in a reference frame attached to the leading bubble), it was expected that the wake dimensions also revealed some sort of variation throughout the bubbles approach sequence to adjust to these hydrodynamic changes. From the observation of Fig. 12, confirming this expectation, it becomes clear that the wake dimensions undergo considerable and

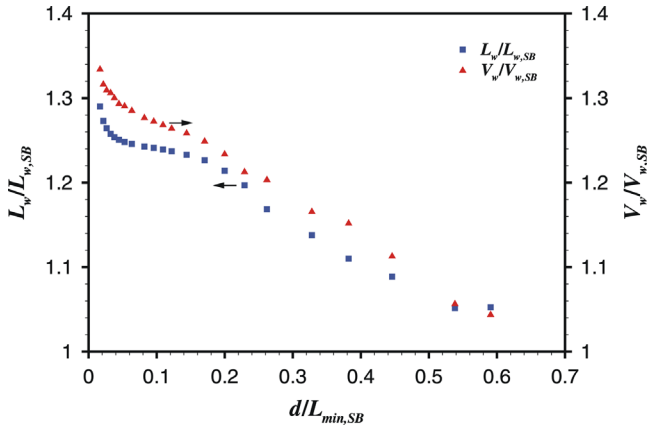


**Fig. 12.** Evolution of the wake dimensions of the trailing bubble with  $d/L_{min,SB}$ , in the form of  $L_w/L_{w,SB}$  and  $V_w/V_{w,SB}$ , obtained for flow condition B.

continuous increments, with a slight preponderance of the normalized wake volume ( $V_w/V_{w,SB}$ ) that, for flow condition B, achieves percentage deviations from  $V_{w,SB}$  up to 33%.

Since it was proven that the wake dimensions of the trailing bubble increase with a decrease in the separation distance between bubbles, the evolution of the values of  $L_w$  and  $V_w$  must also be directly related to the liquid velocity exiting the developed film of the trailing bubble. To inspect and generalize a possible relation, the first step is to normalize the involved features. The wake dimensions were used in the form of  $L_w/D$  and  $V_w/D^3$ , and to express the changes of the liquid velocity in the film, it was used a Reynolds number specific of this flow region ( $Re_\delta$ ) and defined as

$$Re_\delta = \frac{\rho_L U_\delta \delta}{\mu_L} \quad (5)$$

A dependence of the wake dimensions of individual Taylor bubbles, flowing through vertical columns of stagnant liquid, on  $Eo$  and  $M$  is reported in Araújo et al. (2012). This  $L_w/D$  and  $V_w/D^3$  data for single bubbles can be plotted against the corresponding values obtained for the Reynolds number of the film ( $Re_{\delta,SB}$ ), and checked if the evolution of the wake dimensions of the trailing bubble with  $Re_\delta$ , determined by Eq. (5), has a different or similar trend. In this kind of representation, there are two aspects concerning  $Re_\delta$  that must be taken into account. The first one is the fact that the range of  $Re_\delta$  values covered throughout a simulation of a pair of bubbles in a single flow condition is very limited, e.g., in condition B, the  $Re_\delta$  of the trailing bubble varies between 31.3 and 46.3. To extend the comparison with the wake dimensions obtained for single bubbles to a wider range of  $Re_\delta$ , the values of  $L_w/D$  and  $V_w/D^3$  were determined for the simulation data of five different flow conditions with an identical Morton number of  $4.72 \times 10^{-5}$ . The second aspect is a consequence of the MFR used in the simulation method: attaching the frame of reference applied to the leading bubble is necessary to maintain it stationary, but it also implies that the trailing bubble has an upward axial velocity in this MFR, and so, the  $U_\delta$  values placed in Fig. 9 cannot be treated directly as a relative velocity between the trailing bubble and the liquid exiting the film. Since for the  $Re_{\delta,SB}$  results the average velocities in the liquid film were taken for a single bubble immobilized (in a similar MFR), the values of the  $U_\delta$  presented in Fig. 9 should be corrected before using them to calculate the sets of  $Re_\delta$  compatible for comparison with the single bubble data. To implement this change of reference frame into the original  $U_\delta$  simulation data, it is necessary to determine the corresponding values of the trailing bubble in the MFR used. As it is highlighted in Section 3.4, to obtain velocity values that characterize the entire trailing bubble is a complex task, since the position of its extremities is not being

displaced at the same velocity, especially due to a stretching phenomenon already pointed out. In order to tackle this difficulty, since the trailing bubble bottom is the extremity closer to the liquid film, it was used the displacement of the axial coordinate of this gas–liquid interface in this region, measured in the column centreline, to obtain approximate velocity values that were applied in the correction of the  $U_\delta$  data. The resulting sets of  $L_w/D$  and  $V_w/D^3$  against the corrected  $Re_\delta$  are gathered in Fig. 13, together with the corresponding numerical data obtained for single bubbles at a  $M$  of  $4.72 \times 10^{-5}$  (Araújo et al., 2012).

A general observation taken from the graphs in Fig. 13 is that the values of the wake dimensions of the trailing bubble, for the five simulations analysed in detail, are not too far from the trend lines exhibited for  $L_w/D$  and  $V_w/D^3$  as a function of  $Re_\delta$  regarding single bubble systems. With the exception of the points for small separation distances (higher  $Re_\delta$ ) concerning the flow condition with  $M=4.72 \times 10^{-5}$  and  $Eo=34$ , the  $L_w/D$  and  $V_w/D^3$  data compiled in Fig. 13, for systems with a pair of Taylor bubbles, is within an absolute deviation interval of 7% and 13%, respectively, when compared to the corresponding values calculated from the trend lines referent to single bubbles. Although it seems that these trend lines, based on numerical data taken from simulations of isolated Taylor bubbles, can produce reasonable estimations for the values of  $L_w/D$  and  $V_w/D^3$  throughout the main part of the bubbles approach process, it is important to notice that, within each flow condition, the evolution of the wake dimensions of the trailing bubble with  $Re_\delta$  has a distinct behaviour from the referred trend lines. This behaviour presents a non-linear tendency, using a

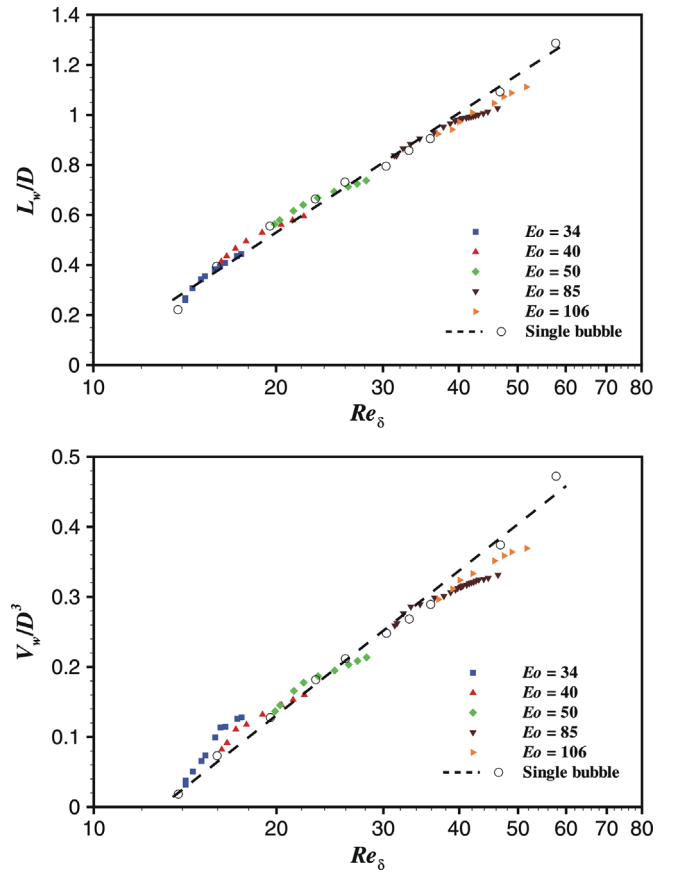


**Fig. 13.** Compilation of numerical data obtained for  $L_w/D$  and  $V_w/D^3$  of the trailing bubble (filled symbols), as a function of  $Re_\delta$ , and regarding the bubbles approach process at different flow conditions within  $M$  of  $4.72 \times 10^{-5}$ . Values of the corresponding features obtained for single bubble systems (Araújo et al., 2012) are also represented (open symbols), together with respective trend line (dashed line).



logarithmic scale in the  $Re_\delta$  axis, and the corresponding deviations from the single bubble trend lines are most probably related to trailing bubble width issues as the bubbles get closer. Based on the data shown in Fig. 9, an increase of the thickness of the trailing bubble developed film is accompanied by an increase in  $Re_\delta$ , contrasting with the simulation results obtained for single bubbles systems where, for the range of  $Eo$  under consideration, a growing tendency of the  $Re_\delta$  is associated with a decrease in the values of  $\delta_{SB}$ .

### 3.4. Velocity ratio

One of the most important features reflecting the disturbed state of a trailing bubble is the velocity ratio between two consecutive Taylor bubbles ( $U/U_{SB}$ ). To obtain this ratio, it was necessary to determine the displacement of the front end position of the trailing bubble, defined in the column axis, from a reference point placed in the leading bubble. There are two possibilities to place this reference point: in the nose or in the tail of the leading bubble. For consistency purposes, both reference locations were defined as the points of intersection between the corresponding interfaces (nose and tail) and the column centreline.

In Fig. 14, the evolution of the numerical results of  $U/U_{SB}$  with the dimensionless separation distance ( $d/D$ ), obtained for both reference points, is directly compared. This comparison is presented for the two flow conditions already placed under the scope in previous sections: condition A— $M=104$  and  $Eo=121$ ; condition B— $M=4.72 \times 10^{-5}$  and  $Eo=85$ .

When looking at Fig. 14, it is clear that, for the flow condition with the lower Morton number, the  $U/U_{SB}$  results are independent of the reference point taken in the leading bubble. However, regarding flow condition A, the choice of the reference point deeply affects the velocity ratio data, which can be confirmed in

the left side of Fig. 14, through the separation of the two  $U/U_{SB}$  curves presented.

To better understand the motive behind this behaviour, the evolution of the bubbles dimensionless length (leading and trailing) with  $d/D$ , for both flow conditions, is shown in Fig. 15. These lengths were obtained as the difference between the nose and tail positions taken at the column axis. In flow condition B, as the separation distance gets smaller, the trailing bubble is considerably stretched up to a length increase around 31%, while the leading bubble maintains its length approximately constant throughout the bubbles approach process. This indicates that the nose and tail reference positions of the leading bubble are more or less stable, which makes the numerical  $U/U_{SB}$  data unaffected by the choice of the reference point. On the other hand, for flow condition A, it is observed a more noticeable variation in the length of the leading bubble (a decrease of around 6.0%) throughout the approximation process. Knowing that the nose position of the leading bubble remains approximately fixed during the simulations, the length decrease is due to a visible upward dislocation of the tail reference point. For this case, the option of the reference point is not irrelevant, justified by a pronounced deformation of the tail of the leading bubble, already pointed out in Section 3.1. So, care should be taken when choosing the point of reference in the leading bubble, since velocity ratio data analysis and interpretation can be severely influenced by this option. Since the interaction of two bubbles is evaluated as depending on the distance between the tail of the leading bubble and the nose of the trailing one, for coherence issues, from this point forward, it was selected the tail of the leading bubble as reference when analysing numerical data involving velocity ratios.

A compilation of the  $U/U_{SB}$  numerical data obtained throughout this work is presented in Fig. 16. The results are divided into five different sets concerning the values of  $M$  under the scope and, within each set, numerical data regarding several Eötvös numbers

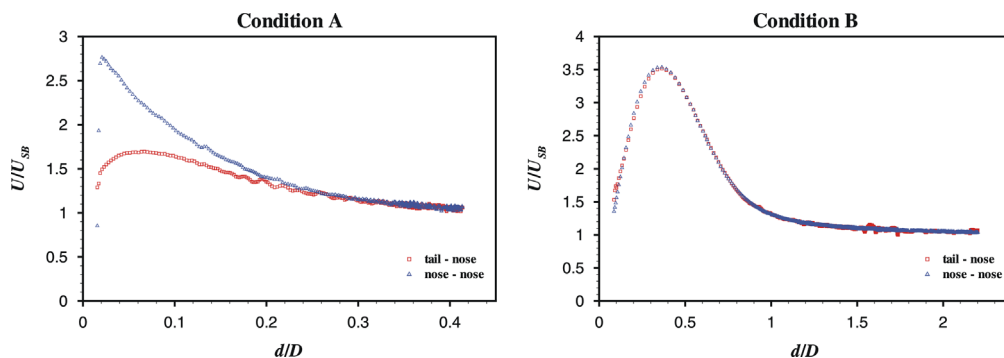


Fig. 14. Comparison of the velocity ratio curves using the nose (nose–nose) and the tail (tail–nose) of the leading bubble as the reference point, regarding flow conditions A ( $M=104$  and  $Eo=121$ ) and B ( $M=4.72 \times 10^{-5}$  and  $Eo=85$ ).

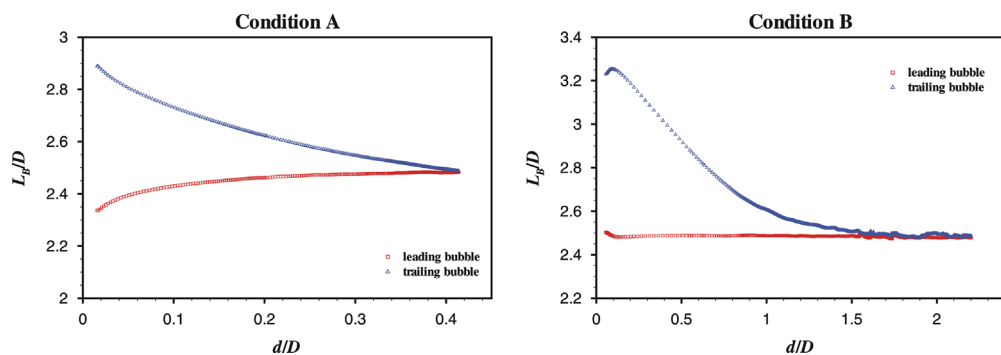


Fig. 15. Evolution of the dimensionless length of the leading and trailing bubbles with  $d/D$  for flow conditions A ( $M=104$  and  $Eo=121$ ) and B ( $M=4.72 \times 10^{-5}$  and  $Eo=85$ ).

is shown. Generally, following the numerical  $U/U_{SB}$  curves in the opposite direction of the horizontal axis ( $d/D$ ), it can be said that, as the trailing bubble approaches the leading one, its velocity ratio grows until exhibiting a maximum and then suffers a decay that seems to tend to one as bubble coalescence is imminent. The only two exceptions from this standard behaviour were obtained for the conditions of  $Eo$  of 15, for both  $M=0.328$  and  $1.64 \times 10^{-2}$ , where the velocity ratio of the trailing bubble increased throughout the entire approach process, although with a very shy intensity.

Looking at Fig. 16, it is also obvious that the referred  $U/U_{SB}$  maximum values and the associated dimensionless distances are highly dependent on the flow conditions, i.e., on Morton and the Eötvös numbers. A simple observation that can be made is that, as  $Eo$  increases or  $M$  decreases, the maximum values of  $U/U_{SB}$  increase. Also, their positions, regarding the horizontal axis shift to the right, which implies that when these maximums occur the normalized distances between the two bubbles are larger. To support this observation, the numerical maximums of the velocity ratio ( $U/U_{SB}|_{max}$ ) and the corresponding dimensionless distances ( $d/D|_{max}$ ), as a function  $Eo$  and  $M$ , are represented in the upper part of Fig. 17.

After analysing in detail the behaviour of the numerical velocity ratio curves in Fig. 16, it was concluded that a standard  $U/U_{SB}$  curve comprises two main regions: acceleration and deceleration. The first region occurs when the bubbles starts to approach, and the trailing bubble is under an accelerating process towards the tail of the leading one. This region ends when the slope of the corresponding  $U/U_{SB}$  curve has reached its maximum value. The acceleration is defined by

$$\text{acceleration} = \frac{U}{U_{SB}} \frac{\partial(U/U_{SB})}{\partial(d/D)} \quad (6)$$

For each flow condition, with the help of Eq. (6), it was determined the dimensionless distance of transition ( $d/D|_{TR}$ ) between the acceleration and deceleration regions of the velocity ratio data. The results obtained are presented in the lower part of Fig. 17, and show a tendency with  $Eo$  and  $M$  similar to  $d/D|_{max}$ .

The acceleration region of the velocity ratio curves was already experimentally identified by several authors, but was never determined for small separation distances, or for such a wide range of flow conditions, within the laminar regime, as it is presented in this work. Based on the work of Moissis and Griffith (1962), Eq. (7) proposes a decreasing exponential functionality

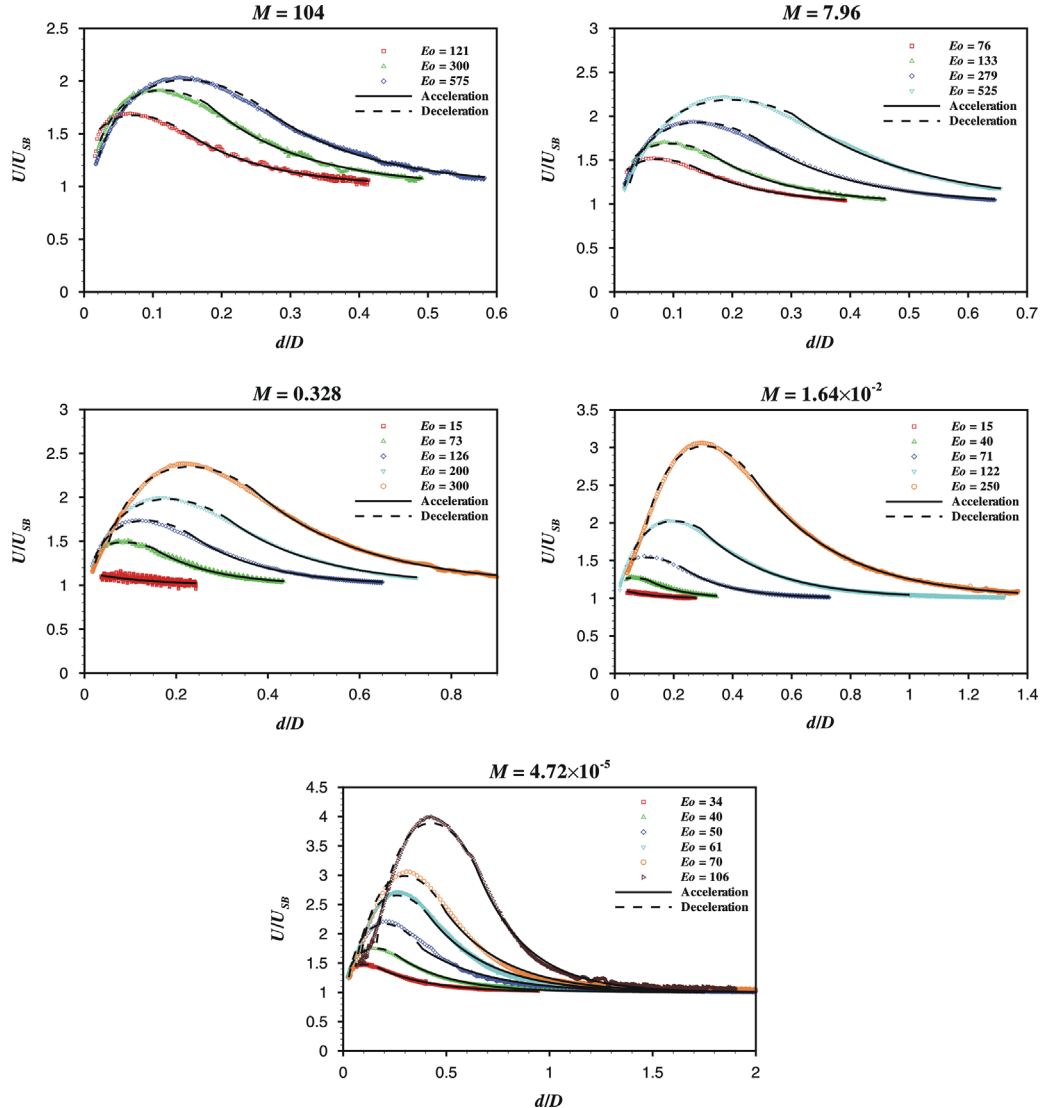


**Fig. 16.** Numerical results of  $U/U_{SB}$  as a function of  $d/D$  (symbols), for a set of five different Morton numbers and several  $Eo$ . The predicted curves for the acceleration (solid lines) and deceleration (dashed lines) regions were also added to all the flow conditions presented.

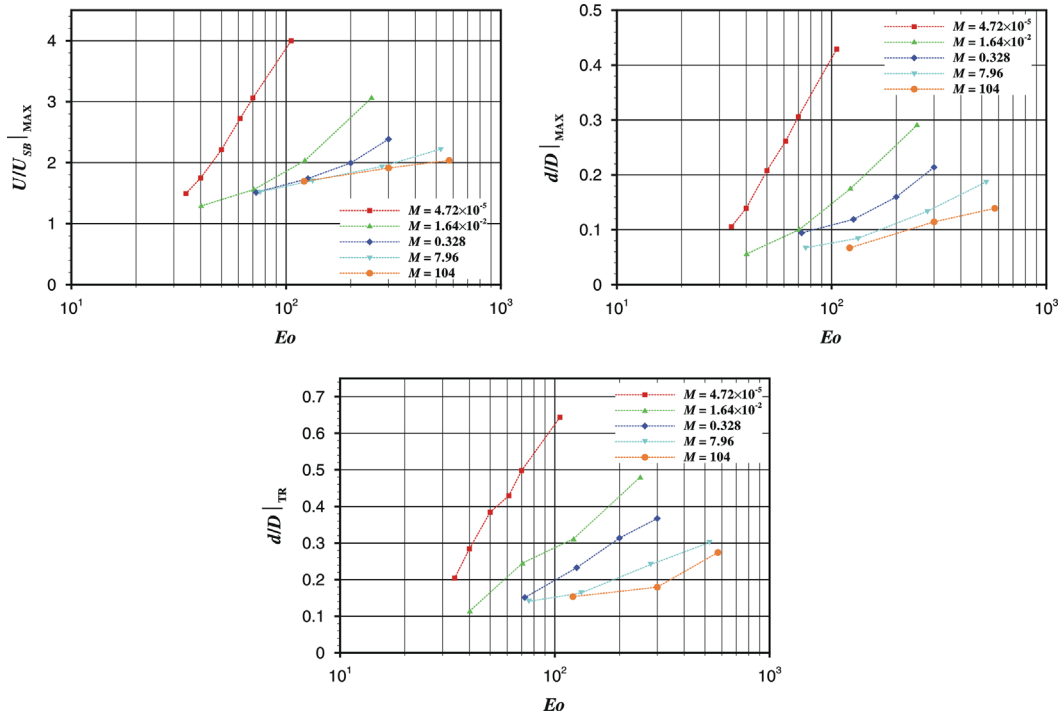


**Fig. 17.** Maximum velocity ratios (upper left graph) and corresponding separation distance (upper right graph) as a function of  $Eo$  and  $M$ . The dependence of  $d/D|_{TR}$  with  $Eo$  and  $M$  is also shown (lower graph). The numerical results are represented by symbols connected with dotted lines to help visualize the tendency of the presented data.

**Table 1**  
Parameters obtained for the definition of the acceleration and deceleration predicting equations.

$M$	$Eo$	Acceleration		Deceleration			
		$a$	$b$	$a'$	$b'$	$c'$	$d/D _{min}$
$4.72 \times 10^{-5}$	34	0.815	3.91	1.36	-17.9	-7.85	0.040
	40	1.75	3.91	0.804	-26.5	-14.4	0.020
	50	2.48	3.13	-0.551	-41.2	-25.8	0.022
	61	5.63	3.51	-4.55	-59.6	-44.4	0.060
	70	7.65	3.45	-8.98	-72.3	-59.9	0.085
	106	30.9	4.15	-31.8	-94.1	-110	0.160
$1.64 \times 10^{-2}$	15	0.141	9.92	–	–	–	–
	40	0.649	8.72	1.33	-13.1	-4.72	0.037
	71	1.82	6.51	1.55	-17.3	-7.75	0.060
	122	3.20	4.27	-0.430	-36.2	-22.5	0.050
	250	8.19	3.47	-9.48	-72.6	-61.1	0.100
0.328	15	0.148	7.65	–	–	–	–
	73	1.34	7.73	1.32	-25.4	-10.4	0.038
	126	2.58	6.47	0.596	-36.4	-18.1	0.017
	200	3.78	5.15	0.047	-36.6	-21.4	0.019
	300	5.18	4.24	-2.08	-48.6	-33.1	0.050
7.96	76	1.36	8.58	1.29	-34.5	-13.3	0.020
	133	1.99	7.63	1.04	-45.0	-19.1	0.031
	279	3.48	6.39	0.116	-48.7	-25.1	0.017
	525	4.58	4.96	-0.638	-44.9	-27.6	0.025
104	121	1.85	8.63	1.52	-45.9	-17.6	0.019
	300	2.94	7.39	0.240	-65.5	-30.1	0.020
	575	4.16	6.61	-0.146	-54.3	-28.4	0.022

between  $U/U_{SB}$  and  $d/D$  to describe the acceleration part of the velocity ratio curves. For each flow condition, the numerical  $U/U_{SB}$  data were adjusted to this equation using  $a$  and  $b$  as fitting parameters.

$$\frac{U}{U_{SB}} = 1 + a \exp\left(-b \frac{d}{D}\right) \quad (7)$$

The complete set of fitted  $a$  and  $b$  values are gathered in the “acceleration” column of Table 1. These values allow us to define an analytical expression, valid for each flow condition studied, that can describe the acceleration region of the  $U/U_{SB}$  curves. To confirm the quality of the fittings, the expressions obtained were also represented in Fig. 16 as solid lines.

The deceleration region is characterized by very small separation distances (lower than  $d/D|_{TR}$ ), and starts when the maximum in the acceleration is achieved. The acceleration then begins to fall and eventually attains negative values for separation distances very close to coalescence. Until now, this deceleration part of the  $U/U_{SB}$  curves was not addressed in the literature. However, it was noted that, for the flow conditions simulated and in the major part of the deceleration region, the acceleration data was reasonably well correlated by a linear functionality with the natural logarithm of  $d/D$ , resulting in the following relation between  $U/U_{SB}$  and  $d/D$ :

$$\frac{U}{U_{SB}} = \sqrt{a' + b' \left(\frac{d}{D}\right) + c' \left(\frac{d}{D}\right) \left[\ln\left(\frac{d}{D}\right) - 1\right]} \quad (8)$$

This expression was used to predict the  $U/U_{SB}$  numerical data in the major part of the deceleration region of the velocity ratio curves obtained here. The values of the fitting parameters  $a'$ ,  $b'$  and  $c'$  were compiled in the “deceleration” column of Table 1, together with the  $d/D$  lower limit of validity. The prediction curves resulting from the combination of Eq. (8) with the parameter values just referred were also added to the graphs of Fig. 16 (dashed lines). The agreement observed is quite reasonable, particularly regarding the  $U/U_{SB}|_{max}$  values and the separation distance where it occurs ( $d/D|_{max}$ ).

It is important to notice that, for the flow conditions studied, the parameters placed in Table 1 together with Eqs. (7) and (8) can be used to describe almost the entire velocity behaviour of a trailing bubble during its merging process with a leading one. This new information can be very useful, since it helps to predict more accurately the hydrodynamics of continuous slug flow and

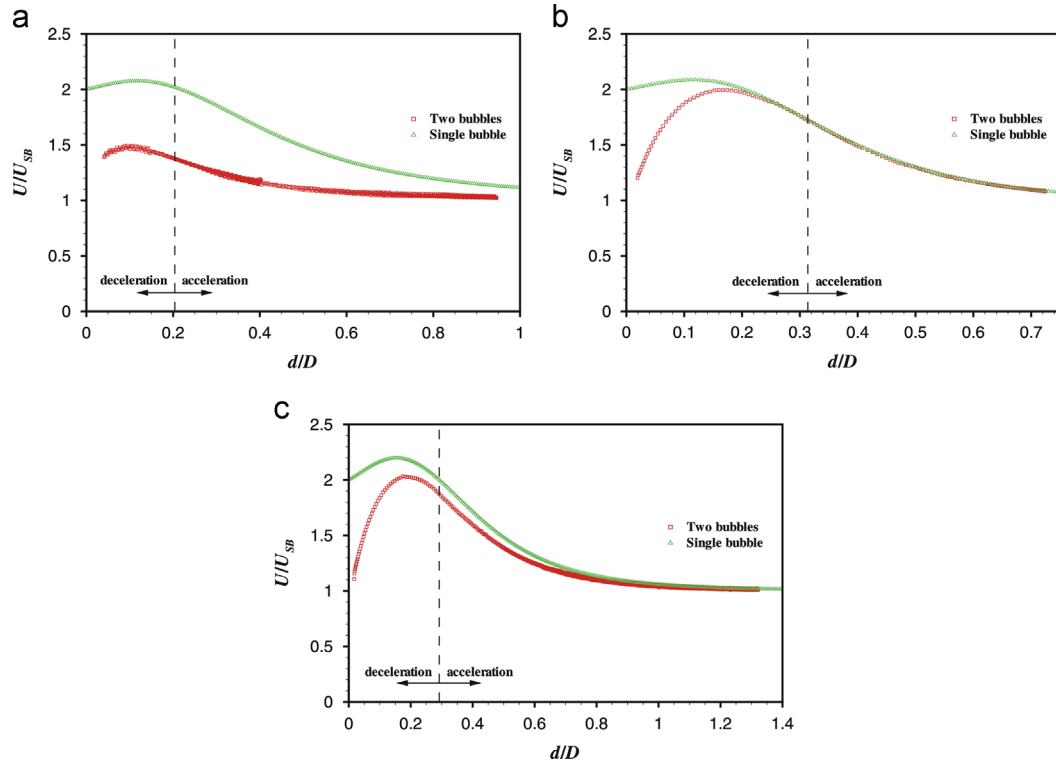


**Fig. 18.** Direct comparison of the  $U/U_{SB}$  results obtained by simulation (two bubbles) with the predictions made with the velocity fields developed in the liquid below of an isolated bubble (single bubble). Three graphs are presented concerning different flow conditions: (a)  $M=4.72 \times 10^{-5}$  and  $Eo=34$ ; (b)  $M=0.328$  and  $Eo=200$ ; and (c)  $M=1.64 \times 10^{-2}$  and  $Eo=122$ .

improves the simulators already developed (van Hout et al., 2001; Mayor et al., 2007a, 2007b, 2008b).

Another possibility that was explored for predicting the  $U/U_{SB}$  curves is based on the velocity field around an individual and undisturbed Taylor bubble rising through a vertical column of stagnant liquid. According to what was already stated before (Sousa et al., 2007), since the rise of an isolated bubble only disturbs the above liquid in a short distance, in similar flow conditions, the velocity field ahead of the nose of a trailing bubble should be close to the one observed in the wake of an isolated bubble. Combining this assumption with the principle that the translational velocity of the trailing bubble can be considered as the superposition of the local liquid velocity immediately ahead of its nose tip with  $U_{SB}$  (Polonsky et al., 1999), it was applied in the following equation:

$$U|_{d/D} = u_z|_{d/D} + U_{SB} \quad (9)$$

where  $U|_{d/D}$  is the rising velocity of the trailing bubble when the distance to the leading one is  $d/D$ , and  $u_z|_{d/D}$  is the liquid axial velocity obtained for the flow of an isolated bubble, and taken in the column axis at the same distance  $d/D$  below its tail. The necessary set of  $u_z|_{d/D}$  data was previously produced by Araújo et al. (2012).

After a first comparison between the  $U/U_{SB}$  simulation results and the velocity ratio data produced from the velocity field of an isolated bubble, the first conclusion was that Eq. (9) is not able to predict the deceleration region of the  $U/U_{SB}$  curves. Focusing this analysis into the acceleration region of the  $U/U_{SB}$  data, it was necessary to assume a quantifiable criterion that could evaluate the predictions of  $U/U_{SB}$  made by Eq. (9). The criterion chosen compared the areas below the simulation  $U/U_{SB}$  curve with the corresponding curve based on the data for an isolated bubble, within the acceleration region previously delimited. If the values

obtained differed less than 10%, it was considered that the prediction made with Eq. (9) is acceptable. All the flow conditions simulated were analysed and, according to the defined criterion, when  $Eo > 90$  and  $M \geq 1.64 \times 10^{-2}$ , the acceleration region of  $U/U_{SB}$  curves can be easily produced by Eq. (9), with a fair degree of proximity to the correct values. For higher Morton numbers (above 7.96), it is even possible to extend the acceptability interval to Eötvös values below 90.

To visualize the effect on the velocity ratio curves of the deviations spectrum encountered in the analysis just described, three illustrative cases are presented in Fig. 18. These cases comprise the one with higher deviation ( $M=4.72 \times 10^{-5}$  and  $Eo=34$ ), the one with higher proximity ( $M=0.328$  and  $Eo=200$ ), and the flow condition with the larger error – 6% – within the acceptability interval ( $M=1.64 \times 10^{-2}$  and  $Eo=122$ ).

#### 4. Conclusions

The main goal of exploiting computational fluid dynamics techniques to describe the rising of two consecutive Taylor bubbles through vertical stagnant Newtonian liquids was achieved. The set of flow conditions simulated cover a wide range of Morton numbers ( $4.72 \times 10^{-5}$ –104) and Eötvös numbers within 15–575, which ensured that all the liquid regions inside the domain were under laminar regime. This study applied a numerical code based on the volume of fluid methodology already included in the commercial package ANSYS FLUENT (Release 12.1.4).

A general overview about the influence of the flow conditions on the bubbles shape and the surrounding liquid flow, during the bubbles approach process, was first presented. It was verified that the nose shape of the trailing bubble is the feature with the most noticeable alterations, particularly for lower values of the Morton number or when the Eötvös number increases. Then, it was performed



a more detailed analysis of the simulation data, regarding two flow conditions on the limits of the interval of  $M$  under investigation (condition A— $M=104$  and  $Eo=121$ ; condition B— $M=4.72 \times 10^{-5}$  and  $Eo=85$ ), based on an inspection about the influence of the separation distance between bubbles on the main hydrodynamic features of the liquid film and wake region of the trailing bubble, and how the shape of the interface extremities behave as the bubbles approach.

Concerning the two extremities directly involved in the coalescence mechanism, it was identified a sharpening-flattening behaviour on the shape of the trailing bubble nose, as the separation distance decreases, and the leading bubble bottom underwent a substantial level of deformation, particularly as the liquid viscosity increases. It was also confirmed that, throughout the bubbles approach process, the nose of the leading bubble remains undisturbed and the shape of the trailing bubble bottom suffers only slight variations.

Due to the changes on the bubbles shape and the drainage of liquid between them, as the approach process evolves, the flow in the developing film of the trailing bubble suffers significant alterations. This fact was proven by the behaviour presented here for the main hydrodynamic features regarding the referred flow region. Among the features addressed are the length necessary to achieve a fully developed film ( $Z'$ ), the liquid film thickness ( $\delta$ ) and the average velocity inside the developed film ( $U_\delta$ ). Generally, all of these features showed a growing tendency, as the separation distance between bubbles gets shorter, although, not only their magnitude increase but also the functionality with  $d/L_{min,SB}$  seems to be highly dependent on the flow conditions used.

The wake dimensions data gathered in this work ( $L_w/D$  and  $V_w/D^3$ ) also reveal an increasing trend throughout the bubbles approach process, where the numerical results concerning flow condition B includes values of  $V_w$  that achieves an increase up to 33% when compared to the corresponding  $V_{w,SB}$ . The evolution of  $L_w/D$  and  $V_w/D^3$  of the trailing bubble with the Reynolds number in the film is also presented for a set of flow conditions, within the Morton number of  $4.72 \times 10^{-5}$ , and are shown together with corresponding data for single bubble systems (Araújo et al., 2012). Although distinct behaviours between the tendencies of the wake dimensions with  $Re_\delta$  for single and two bubbles systems are noticed, it is important to emphasize that the deviations are not excessive. As it was expected, the results of the increase in the stabilization length below the trailing bubble compared to  $L_{min,SB}$ , for flow condition B, are similar to those presented for  $U_\delta/U_{\delta,SB}$ .

Numerical data on the velocity ratio between the leading and the trailing bubble was produced for a wide range of flow conditions, including results for very small separation distances. Two regions were identified in the  $U/U_{SB}$  curves – acceleration and deceleration – and equations together with values of fitting parameters are proposed to describe these two regions. In the future, the purpose is to couple this kind of information with models used in simulators of continuous slug flow. Finally, it was also shown that the acceleration region of the  $U/U_{SB}$  curves can be predicted from corresponding data obtained for single bubble systems when  $Eo > 90$  and  $M \geq 1.64 \times 10^{-2}$ .

## Acknowledgements

The authors gratefully acknowledge the financial support from the Foundation for Science and Technology (FCT) through the project PTDC/EQU-FTT/69068/2006 and grant SFRH/BPD/64148/2009. POCTI (FEDER) also supported this work via CEFT.

## References

- Aladjem Talvy, C., Shemer, L., Barnea, D., 2000. On the interaction between two consecutive elongated bubbles in a vertical pipe. *Int. J. Multiphase Flow* 26, 1905–1923.
- Araújo, J.D.P., Miranda, J.M., Pinto, A.M.F.R., Campos, J.B.L.M., 2012. Wide-ranging survey on the laminar flow of individual Taylor bubbles rising through stagnant Newtonian liquids. *Int. J. Multiphase Flow* 43, 131–148.
- Asadolahi, A.N., Gupta, R., Fletcher, D.F., Haynes, B.S., 2011. CFD approaches for the simulation of hydrodynamics and heat transfer in Taylor flow. *Chem. Eng. Sci.* 66, 5575–5584.
- Barnea, D., Taitel, Y., 1993. A model for slug length distribution in gas–liquid slug flow. *Int. J. Multiphase Flow* 19, 829–838.
- Bendiksen, K., 1985. On the motion of long bubbles in vertical tubes. *Int. J. Multiphase Flow* 11, 797–812.
- Brackbill, J.U., Kothe, D.B., Zemach, C., 1992. A continuum method for modeling surface tension. *J. Comput. Phys.* 100, 335–354.
- Brill, J.P., Mukherjee, H., 1999. *Multiphase Flow in Wells*. Society of Petroleum Engineers Inc., USA.
- Campos, J.B.L.M., Guedes de Carvalho, J.R.F., 1988a. An experimental study of the wake of gas slugs rising in liquids. *J. Fluid Mech.* 196, 27–37.
- Campos, J.B.L.M., Guedes de Carvalho, J.R.F., 1988b. Mixing induced by air slugs rising in narrow columns of water. *Chem. Eng. Sci.* 43, 1569–1582.
- Chinnov, E.A., Kabov, O.A., 2006. Two-phase flows in pipes and capillary channels. *High Temp.* 44, 773–791.
- Collins, R., de Moraes, F.F., Davidson, J.F., Harrison, D., 1978. The motion of a large gas bubble rising through liquid flowing in a tube. *J. Fluid Mech.* 89, 497–514.
- Davies, R.M., Taylor, G., 1950. The mechanics of large bubble rising through extended liquids and through liquids in tubes. *Proc. R. Soc. London A* 200, 375–390.
- Dumitrescu, D.T., 1943. Strömung an einer Luftblase im Senkrechten Rohr. *Z. Angew. Math. Mech.* 23, 139–149.
- Goldsmith, H.L., Mason, S.G., 1962. The movement of single large bubbles in closed vertical tubes. *J. Fluid Mech.* 14, 52–58.
- Gupta, R., Fletcher, D.F., Haynes, B.S., 2009. On the CFD modelling of Taylor flow in microchannels. *Chem. Eng. Sci.* 64, 2941–2950.
- Gupta, R., Fletcher, D.F., Haynes, B.S., 2010. CFD modelling of flow and heat transfer in the Taylor flow regime. *Chem. Eng. Sci.* 65, 2094–2107.
- Hirt, C.W., Nichols, B.D., 1981. Volume of fluid (VOF) method for the dynamics of free boundaries. *J. Comput. Phys.* 39, 201–225.
- James, M.R., Lane, S.J., Chouet, B., Gilbert, J.S., 2004. Pressure changes associated with the ascent and bursting of gas slugs in liquid-filled vertical and inclined conduits. *J. Volcanol. Geotherm. Res.* 129, 61–82.
- Leung, S.S.Y., Liu, Y., Fletcher, D.F., Haynes, B.S., 2010. Heat transfer in well-characterised Taylor flow. *Chem. Eng. Sci.* 65, 6379–6388.
- Mao, Z.S., Duckler, A., 1991. The motion of Taylor bubbles in vertical tubes: II. Experimental data and simulations for laminar and turbulent flow. *Chem. Eng. Sci.* 46, 2055–2064.
- Mayor, T.S., Pinto, A.M.F.R., Campos, J.B.L.M., 2007a. Hydrodynamics of gas–liquid slug flow along vertical pipes in the laminar regime—experimental and simulation study. *Ind. Eng. Chem. Res.* 46, 3794–3809.
- Mayor, T.S., Pinto, A.M.F.R., Campos, J.B.L.M., 2007b. Hydrodynamics of gas–liquid slug flow along vertical pipes in turbulent regime—a simulation study. *Chem. Eng. Res. Des.* 85, 1497–1513.
- Mayor, T.S., Ferreira, V., Pinto, A.M.F.R., Campos, J.B.L.M., 2008a. Hydrodynamics of gas–liquid slug flow along vertical pipes in turbulent regime—an experimental study. *Int. J. Heat Fluid Flow* 29, 1039–1053.
- Mayor, T.S., Pinto, A.M.F.R., Campos, J.B.L.M., 2008b. Vertical slug flow in laminar regime in the liquid and turbulent regime in the bubble wake—comparison with fully turbulent and fully laminar regimes. *Chem. Eng. Sci.* 63, 3614–3631.
- Mercier, M., Fonade, C., Lafforgue-Delorme, C., 1997. How slug flow can enhance the ultrafiltration flux in mineral tubular membranes. *J. Membr. Sci.* 128, 103–113.
- Moissis, R., Griffith, P., 1962. Entrance effects in a two-phase slug flow. *J. Heat Transfer* 84, 29–39.
- Nešić, S., 2007. Key issues related to modelling of internal corrosion of oil and gas pipelines—a review. *Corros. Sci.* 49, 4308–4338.
- Nicklin, D.J., Wilkes, J.O., Davidson, J.F., 1962. Two-phase flow in vertical tubes. *Trans. Inst. Chem. Eng.* 40, 61–68.
- Nogueira, S., Riethmüller, M.L., Campos, J.B.L.M., Pinto, A.M.F.R., 2006. Flow patterns in the wake of a Taylor bubble rising through vertical columns of stagnant and flowing Newtonian liquids: an experimental study. *Chem. Eng. Sci.* 61, 7199–7212.
- Pangarkar, K., Schildhauer, T.J., van Ommen, J.R., Nijenhuis, J., Kapteijn, F., Moulijn, J.A., 2008. Structured packing for multiphase catalytic reactors. *Ind. Eng. Chem. Res.* 47, 3720–3751.
- Pinto, A.M.F.R., Campos, J.B.L.M., 1996. Coalescence of two gas slugs rising in a vertical column of liquid. *Chem. Eng. Sci.* 51, 45–54.
- Pinto, A.M.F.R., Coelho Pinheiro, M.N., Campos, J.B.L.M., 1998. Coalescence of two gas slugs rising in a co-current flowing liquid in vertical tubes. *Chem. Eng. Sci.* 53, 2973–2983.
- Polonsky, S., Shemer, L., Barnea, D., 1999. The relation between the Taylor bubble motion and the velocity field ahead of it. *Int. J. Multiphase Flow* 25, 957–975.
- Ratkovich, N., Berube, P.R., Nopens, I., 2011. Assessment of mass transfer coefficients in coalescing slug flow in vertical pipes and applications to tubular airlift membrane bioreactors. *Chem. Eng. Sci.* 66, 1254–1268.

- Shemer, L., Gulitski, A., Barnea, D., 2007a. On the turbulent structure in the wake of Taylor bubbles rising in vertical pipes. *Phys. Fluids* 19, 035108.
- Shemer, L., Gulitski, A., Barnea, D., 2007b. Movement of two consecutive Taylor bubbles in vertical pipes. *Multiphase Sci. Technol.* 19, 99–120.
- Sousa, R.G., Pinto, A.M.F.R., Campos, J.B.L.M., 2007. Interaction between Taylor bubbles rising in stagnant non-Newtonian fluids. *Int. J. Multiphase Flow* 33, 970–986.
- Taha, T., Cui, Z.F., 2002. CFD modelling of gas-sparged ultrafiltration in tubular membranes. *J. Membr. Sci.* 210, 13–27.
- Talimi, V., Muzychka, Y.S., Kocabiyik, S., 2012. A review on numerical studies of slug flow hydrodynamics and heat transfer in microtubes and microchannels. *Int. J. Multiphase Flow* 39, 88–104.
- van Hout, R., Barnea, D., Shemer, L., 2001. Evolution of statistical parameters of gas–liquid slug flow along vertical pipes. *Int. J. Multiphase Flow* 27, 1579–1602.
- van Hout, R., Gulitski, A., Barnea, D., Shemer, L., 2002a. Experimental investigation of the velocity field induced by a Taylor bubble rising in stagnant water. *Int. J. Multiphase Flow* 28, 579–596.
- van Hout, R., Barnea, D., Shemer, L., 2002b. Translational velocities of elongated bubbles in continuous slug flow. *Int. J. Multiphase Flow* 28, 1333–1350.
- van Hout, R., Shemer, L., Barnea, D., 2003. Evolution of hydrodynamic and statistical parameters of gas–liquid slug flow along inclined pipes. *Chem. Eng. Sci.* 58, 115–133.
- Villarreal, J., Laverde, D., Fuentes, C., 2006. Carbon-steel corrosion in multiphase slug flow and CO<sub>2</sub>. *Corros. Sci.* 48, 2363–2379.
- White, E.T., Beardmore, R.H., 1962. The velocity of rise of single cylindrical air bubbles through liquids contained in vertical tubes. *Chem. Eng. Sci.* 17, 351–361.
- Xia, G.-D., Cui, Z.Z., Liu, Q., 2009. A model for liquid slug length distribution in vertical gas–liquid slug flow. *J. Hydrodyn.* 21, 491–498.
- Youngs, D.L., 1982. Time-dependent multi-material flow with large fluid distortion. In: Morton, K.W., Baibnes, M.J. (Eds.), *Numerical Methods for Fluid Dynamics*. Academic Press, New York.
- Zheng, D., Che, D., 2006. Experimental study on hydrodynamic characteristics of upward gas–liquid slug flow. *Int. J. Multiphase Flow* 32, 1191–1218.